

# Generalizing Energy-based Generative ConvNets from Particle Evolution Perspective

Yang Wu, Pengxu Wei, Xu Cai, Guanbin Li, and Liang Lin

**Abstract**—Compared with Generative Adversarial Networks (GAN), the Energy-Based generative Model (EBM) possesses two appealing properties: i) it can be directly optimized without requiring an auxiliary network during the learning and synthesizing; ii) it can better approximate underlying distribution of the observed data by learning explicitly potential functions. This paper studies a branch of EBMs, *i.e.*, the energy-based Generative ConvNet (GCN), which minimizes its energy function defined by a bottom-up ConvNet. From the perspective of particle physics, we solve the problem of unstable energy dissipation that might damage the quality of the synthesized samples during the maximum likelihood learning. Specifically, we establish a connection between FRAME model [1] and dynamic physics process and provide a generalized formulation of FRAME in discrete flow with a certain metric measure from particle perspective. To address KL-vanishing issue, we generalize the reformulated GCN from the KL discrete flow with KL divergence measure to a Jordan-Kinderlehrer-Otto (JKO) discrete flow with Wasserstein distance metric and derive a Wasserstein GCN (w-GCN). To further minimize the learning bias and improve the model generalization, we present a Generalized GCN (GGCN). GGCN introduces a hidden space mapping strategy and employ a normal distribution as hidden space for the reference distribution. Besides, it applies a matching trainable non-linear upsampling function for further generalization. Considering the limitation of the efficiency problem in MCMC based learning of EBMs, an amortized learning are also proposed to improve the learning efficiency. We learn the GGCN with a symmetrical learning strategy. Quantitative and qualitative experiments are conducted on several widely-used face and natural image datasets. Our experimental results surpass those of the existing models in both model stability and the quality of generated samples. The source code of our work is publicly available at <https://github.com/uiyo/GeneralizedGCN>.

**Index Terms**—FRAME models, energy-based model, generative ConvNets, KL divergence, JKO discrete flow.

## 1 INTRODUCTION

UNSUPERVISED learning of complex data distributions and sample generation are being extensively researched in the machine learning and computer vision community [2], [3], [4]. Generative modeling learns the underlying data distribution given a quantity of data observations. A well-learned generative model can synthesize data samples similar to real-world ones; doing so is thus regarded as the ability to imitate human creativity. There mainly exist two types of representative generative models – either likelihood-free models such as Generative Adversarial Networks (GANs) [5] or likelihood-based models such as Variational AutoEncoders (VAEs) [6] and flow-based model [7]. Another remarkable likelihood-based model, Energy-Based Model (EBM) [8], presents an appealing property that captures the dependencies among variables by evolving a scalar energy to each variable and requires no proper probabilistic normalization.

Compared with GAN, which generates samples by applying a generator and a discriminator learned adversarially, EBM can be directly optimized without any auxiliary; by learning with explicit potential function, it approximates the observed data distribution more closely and hence synthesizes more authentic samples. EBM has the merits of, compared with VAEs, enabling optimization of the exact log-likelihood of the data instead of its lower bound, and, compared with flow-based models, the ability of using the learned model as a prior model for image processing, *e.g.*, by transforming it into a discriminative Convolutional Neural Network (CNN) [9] for classification.

One well-exploited EBM model is a generative energy-based convolutional neural network, also known as

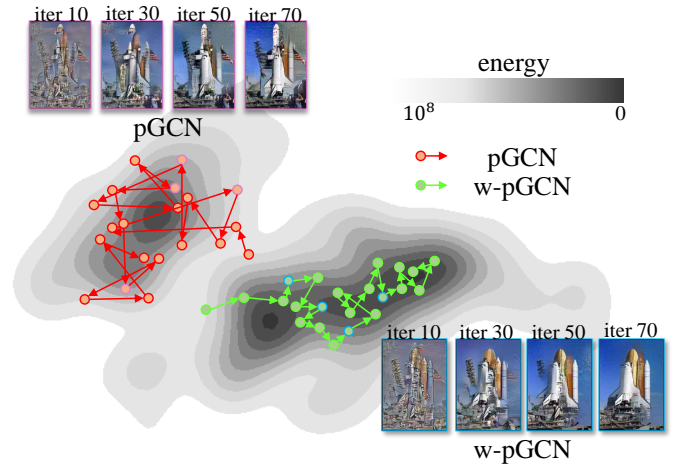


Fig. 1. Learning evolution visualization of pGCN and w-pGCN. The contour map with particles in this figure is an energy dissipation process simulation of both algorithms from the particle perspective. Image sequences are the generating steps and selected typical results for a “spaceship” obtained by pGCN and w-pGCN, respectively. The w-pGCN algorithm produces higher-quality images than pGCN which collapses at the very beginning of the sampling iteration. The process of pGCN manifests seriously unstable when suffering from model collapse, while the dissipation process of w-pGCN is more orderly and ends up with closer to 0 energy point.

GCN [10]. GCN stems from Filters, Random fields, And Maximum Entropy (FRAME) [11] model, which is proposed long before the popularity of deep learning and aims at modeling the texture context. To deal with more complex and high-dimensional sample synthesis, FRAME incorporates deep convolutional network filters and derives a deep

variant of FRAME [12]. This deep FRAME model is identified as prototype GCN (pGCN) in this paper for theoretical simplicity. Regarded as a hierarchical version of pGCN, GCN [10] manages to present the generative property of a discriminative CNN (without another auxiliary network). Considering an EBM usually needs to use Markov chain Monte Carlo (MCMC) to sample from logarithmic partition functions, hence to further solve the difficulty of MCMC on traversing different modes, a multi-scale GCN (M-GCN) [13] is proposed and synthesizes the samples from small and coarse grids to a fine grid.

Essentially, these energy-based GCN models derived from pGCN, which follow the maximum entropy principle (MEP), could be cast into a learning problem of information-theoretical KL divergence between the real-world data distribution  $\mathbb{P}_r$  and the model distribution  $P_\theta$ . With MCMC dynamic discrete sampling, this learning process of minimizing the KL divergence indicates that the learning gradient of each step approximately follows the gradient of a KL discrete flow. In our work, we generalize this KL discrete flow with KL distance measure and accordingly reformulate pGCN from a particle perspective. As for particle perspective, we regard all the samples as a group of disordered dynamic particles and the learning process can be compared to the evolution of particles with a discrete flow (driven by KL divergence, thus known as KL discrete flow) at each learning time step. We also provide theoretical proofs on this equivalence from two viewpoints.

However, energy-based GCN models solve an intractable energy function by a step-by-step iterative MCMC sampling and updating. This solving mechanism exhibits a quite unstable learning and thus tends to generate blurry and twisted images or even ones with crashing contexts. As shown in Fig.1, pGCN model tends to generate collapsed images marked in red, indicating a severe model collapse problem. Considering the synthesis process as an energy dissipation, the energy states of pGCN suffer from quite a mess and end up with a wrong non-zero energy location in the contour map. From the particle perspective, it is more intuitive that the unstable learning process is mainly caused by a KL-vanishing problem. Thus in our proposed w-pGCN, KL discrete flow is substituted by a Jordan-Kinderlehrer-Otto (JKO) discrete flow [14] with a Wasserstein distance measure. As shown in Fig.1, the particles of our proposed w-pGCN evolve more orderly and stably converge to 0 energy location.

Inheriting this JKO discrete flow, we further generalize seamlessly the pGCN with it and derive our Generalized Generative ConvNet Model (GGCN). This generalization strategy is non-trivial, rather than simply replacing pGCN with GCN. In GCN, on one hand, strong dependency on observed data limits the model learning ability and flexibility; on another hand, the MCMC sampling limits the learning efficiency and this would become rigorous for M-GCN whose learning time grows massively with grids of sampling process in different scales.

To address these issues, our proposed GGCN rooted in M-GCN extends its reference distribution to a hidden space and proposes a trainable non-linear upsampling function to mimic the grid-by-grid upscale and sampling process. It avoids the decreasing of synthesis quality caused by

accumulating errors among multi-grid and further improve the model generalization ability.

Iterative learning of several components in GGCN is an urgent problem. We present a symmetrical learning strategy which contains two similar sub-learning processes. One is learning the GCN that synthesis by sampling; the other is learning non-linear upsampling function together with the hidden space by generating. Considering the limitation of the efficiency problem in MCMC based learning of EBMs, it still suffers from a serious time-consuming problem when sampling steps increase. This is the main reason that so far EBMs are rarely trained on large-scale datasets. Accordingly, inspired by the efficient variational reasoning [15], we employ a similar amortized learning method to further shorten the sampling process of GGCN.

In summary, our contributions are as follows:

- We reformulate classical energy-based GCN models from its traditional information theory viewpoint to a particle evolution perspective. Under this particle perspective, a KL discrete flow of learning GCN can be substituted by a JKO discrete flow driven by Wasserstein distance in a principle manner. The derived w-pGCN model with Wasserstein distance measure no longer suffers from KL vanishing problem.
- We further generalize the pGCN with JKO discrete flow and derive our Generalized Generative ConvNet Model. Non-linear upsampling functions are introduced to reduce the sampling steps and thus improve the efficiency and generalization of GCN. Moreover, the original initial reference distribution in M-GCN is modified to a normal distribution which can be regarded as a hidden space. Furthermore, by learning the hidden space, we make the whole model learned in a symmetrical mechanism. An amortized sampling method is also introduced for GGCN to further accelerate its MCMC sampling process.
- Extensive experiments are conducted on several large-scale datasets for image generation tasks, demonstrating the improvements on the generation of proposed models quantitatively and qualitatively.

## 2 RELATED WORK

Generative EBM originating from statistical physics explicitly defines the probability distributions of the signal; in that context, they are ordinarily called the Gibbs distributions [16]. With the extensive development of CNNs that have been proven to be powerful discriminators, the generative perspective on this model has recently been extensively explored by an increasing number of studies. [17] is the first study to introduce a generative gradient for pretraining a discriminative ConvNet by a nonparametric importance sampling scheme, and [12] proposes learning FRAME using pretrained filters of a modern CNN. [10] further studies the theory of GCN in-depth and shows that the model has a unique internal autoencoding representation where the filters in the bottom-up operation take up a new role as the basis functions in the top-down representation, which is consistent with the pGCN model. In this paper, a pGCN model and its variants such as GCN and multi-scale GCN

described above share the same MLE-based learning mechanism that follows an analysis-by-synthesis approach and first generates synthesized samples from the current model using Langevin dynamics (LD) and subsequently learns the parameters based on the distance between observed and synthesized samples.

A preliminary version of our work was published in [18], which also explains the pGCN from the particle evolution perspective. However, we further generalize seamlessly the pGCN with the JKO discrete flow and derive our Generalized Generative ConvNet Model (GGCN) in this paper. GGCN extends its reference distribution to a hidden space to alleviate the dependency of limited observed data and proposes a trainable non-linear upsampling function together with an amortized sampling method to improve learning efficiency. Briefly, the proposed GGCN improves the learning flexibility and model generalization.

Another popular branch of deep generative models is black-box or implicit models that map between some simple low-dimensional prior and complex high-dimensional signals via a top-down deep neural network, such as the GANs, VAEs, flow-based models and their variants. These models have been remarkably successful in generating realistic images. GANs and VAEs are trained together with an assisting model, where VAEs try to optimize the evidenced lower bound that causes them to generate images that are fairly blurry in practical terms, while training GANs entails instability due to the difficulty of finding the exact Nash equilibrium [19], the lack of latent-space encoders and the difficulty of assessing overfitting or memorization [20]. On the other hand, flow-based models either cannot be trained efficiently by maximum likelihood [21], or have poor performance [7], [22].

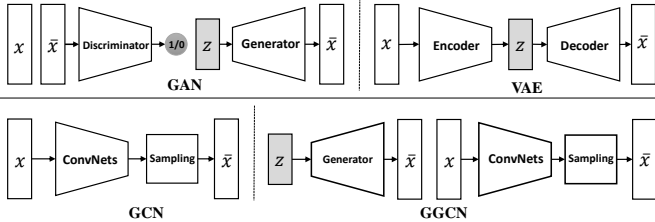


Fig. 2. Comparisons of four categories of generative models on framework. The right downside GGCN model is one of our presented models.

We provide guidelines in Fig.2 to briefly illustrate the relations in the leaning framework among those generative models. Unlike the majority of implicit generative models that use an auxiliary network to guide the training of the generator, energy-based generative models maintain a single model that simultaneously serves as a discriminator and a generator. The latter models generate samples directly from the input data rather than from the latent space, which to a certain extent ensures that the model can be efficiently trained and can produce stable synthesized results with a relatively lower complexity of model structure. Nonetheless, such a model can also be used as an auxiliary model and combined with an implicit model to facilitate the model training [15], [23], [24]. Technically, the learning mechanism of our new symmetrically learned GCN is more similar to cooperative learning [23] as a result of

all parameter estimation steps having one goal in common: to make  $P_\theta$  approximate  $\mathbb{P}_r$ , but considering it is derived by generalizing a single GCN, we entail this new model a generalized GCN model (GGCN). GGCN also implements a generator co-existing with GCN, but unlike GAN of which the discriminator is to confront the generator, the generator introduced is to generalize the base GCN in GGCN.

### 3 REVISITING PROTOTYPE GCN MODEL FROM PARTICLE EVOLUTION PERSPECTIVE

Considering the dynamic learning of conventional pGCN, we regard all the samples as highly disorder dynamic particles in the data space which therefore contains literally physical energy. Real data samples are located where the energy is zero, which can be namely regarded as those particles in a stable state. The learning procedure can be equivalently compared to a process that randomly initialized particles with high energy are gradually led to the low-energy states. The force which leads the particles can be step-by-step modified by estimating the current states of the particles. In consideration of the time dimension, it can be easily imagined that the dynamic particles in discrete time points drift as flows or streams. With this thought, we attempt to reformulate pGCN from this particle evolution perspective. Furthermore, the particle based pGCN reformulation derives theoretically the same updating mechanism as pGCN, which could guarantee the generalization of pGCN and GCN principally.

In this section, we will revisit the GCN with a particle evolution perspective. Theoretical deduction and proposition will be illustrated merely based on pGCN, since all the proposed methods will not involve essential theory modification. Hence the particle perspective and all the new learning strategies can be applied to any form of GCN.

#### 3.1 Prototype Generative ConvNet Model

Based on an energy function, pGCN is defined on the exponential tilt of a gaussian reference distribution  $q$ , which is a reformulation of MRF [12] and can be written as following Gibbs distribution:

$$P(\mathbf{x}; \boldsymbol{\theta}) = \frac{1}{Z(\boldsymbol{\theta})} \exp \left\{ \sum_{k=1}^K \sum_{\mathbf{x} \in \mathcal{X}} \theta_k h(\langle \mathbf{x}, \mathbf{w} \rangle + \mathbf{b})_k \right\} q(\mathbf{x}), \quad (1)$$

where  $h(\mathbf{x}) = \max(0, \mathbf{x})$  is a nonlinear activation function for an input  $\mathbf{x} \in \mathcal{X}$ ,  $\theta_k$  is the  $k$ th element of  $K$ -dimensional model parameter  $\boldsymbol{\theta}$ ,  $\mathbf{w}$  is the parameters of filters and  $\mathbf{b}$  is the bias;  $\langle \mathbf{x}, \mathbf{w} \rangle$  denotes a filtered image or a feature map;  $q(\mathbf{x}) = \frac{1}{(2\pi\sigma^2)^{|\mathcal{X}|/2}} \exp \left[ -\frac{1}{2\sigma^2} \|\mathbf{x}\|^2 \right]$ , which denotes the Gaussian white noise model with mean 0 and variance  $\sigma^2$ ;  $Z(\boldsymbol{\theta})$  is the potential function.

The learning process of a pGCN model (similar to that of MRF models) follows the iterative MLE parameter estimation that firstly updates model parameters by trying to increase the log likelihood  $\log P(\mathbf{x}; \boldsymbol{\theta})$  and subsequently samples from the current distribution using parallel MCMC chains. Assuming that  $\theta_t$  is the parameter of sampled probability distribution at time  $t$ , the sampling process, according to [25], does not necessarily converge at each  $\theta_t$ . We here

provide one persistent sampler that converges globally to reduce the number of calculations, through which we can get numerical solution of the  $\theta$ :

$$\frac{\partial}{\partial \theta_k} \frac{1}{N} \log P(\mathbf{x}; \theta) = \mathbb{E}_{\mathbb{P}_r}[f_k(\mathbf{x})] - \mathbb{E}_{P(\mathbf{x}; \theta)}[f_k(\mathbf{x})], \quad (2)$$

where  $f_k(\mathbf{x})$  in  $\mathbb{E}_{\mathbb{P}_r}[f_k(\mathbf{x})]$  and  $\mathbb{E}_{P(\mathbf{x}; \theta)}[f_k(\mathbf{x})]$  are the feature responses over the real-world data distribution  $\mathbb{P}_r$  and the model distribution  $P(\mathbf{x}; \theta)$ , respectively. According to [12],  $\theta$  above is estimated with LD which injects noise into the parameter updates. A GCN can be considered as a pGCN with trainable deep filters. The parameter  $\mathbf{w}$  is estimated by following equation:

$$\mathbf{w}_{t+1} = \mathbf{w}_t + \nabla_{\mathbf{w}} \mathbb{E}_{P_t}[\Phi(\mathbf{x}; \theta, \mathbf{w}_t)] - \nabla_{\mathbf{w}} \mathbb{E}_{\mathbb{P}_r}[\Phi(\mathbf{x}; \theta, \mathbf{w}_t)], \quad (3)$$

where the  $P_t$  is the estimated data distribution at each sampling step.

Inherently, in energy-based models, this learning and sampling process characterizes an evolution in a state space associated with learning gradients; Inspired by the gradient flow derived from energy models [26], it essentially can be further regarded as an evolution of well-established derivations of stochastic particle model equations, where  $\mathbf{x}$  could be considered as Brownian particles. This gradient flows has proven useful in solving theoretically and numerically diffusion equations that model porous media or crowd evolution [27]. For pGCN, the learning gradient of each step approximately follows a discrete gradient flow, which is named discrete flow for short, and allows us to attach a precise interpretation to the conventional energy-based model from traditional information and statistical theory to particle perspective.

### 3.2 Revisit pGCN from Particle Evolution Perspective

From a particle evolution perspective, we establish a connection between pGCN and dynamic physics process and provide a generalized formulation of pGCN in discrete flow with a certain metric measure. Especially, pGCN follows a discrete flow with KL divergence measure as its objective of minimizing the KL divergence between  $P_\theta$  and  $\mathbb{P}_r$ ; its entire optimization process can be regarded as a particle evolution.

Herein we reformulate pGCN in the context of a KL discrete flow. Namely, dynamic sampling and updating equations of pGCN will be derived in this section, only based on the discrete flow theory. The discrete flow is related to discrete probability distributions (evolution discretized in time) of finite-dimensional problems. More precisely, it represents the system of  $n$  independent Brownian particles  $\{\mathbf{x}_i^j\}_{i=1}^n \in \mathbb{R}^d$ , the positions of which in  $\mathbb{R}^d$  given by a Wiener process (or Brownian motion, a stochastic process of moving particles) satisfy the following stochastic differential equation (SDE):

$$d\mathbf{x}_t = \mu(\mathbf{x}_t)dt + \varepsilon(\mathbf{x}_t)d\mathbf{B}_t, \quad (4)$$

where  $\mu$  is the drift term, the index  $i$  of  $\mathbf{x}$  is left out for simplicity,  $\varepsilon$  represents the diffusion term,  $\mathbf{B}$  denotes the Wiener process, and subscript  $t$  denotes values at time  $t$ . An empirical measure  $\rho_t$ , which is of those particles and proven to approximate Eq. 1 by an implicit descent step

$\rho^* = \operatorname{argmin}_{\rho} \mathcal{I}_t$ .  $\mathcal{I}_t$  is the so-called KL discrete flow at time  $t$  that consists of the KL divergence  $\mathcal{K}$  and energy function  $\Phi: \mathbb{R}^d \rightarrow \mathbb{R}$ ,

$$\mathcal{I}_t = \mathcal{K}(\rho | \rho_t) + \int \Phi d\rho. \quad (5)$$

The connotation of a KL discrete flow that describes a system of Brownian particles with probability distributions inspires a brand new perspective on interpreting a GCN model in the discrete state. If we regard the observed signals  $\{\mathbf{x}_i^j\}_{i=1}^n$  with the generating function that has the Markov property as Brownian particles, we will prove a Theorem 1 which implies that LD in Eq.2 can be deduced from a KL discrete flow for learning pGCN. This theorem can be sufficiently and necessarily proved through Lemma 1. The detailed proof of Theorem 1 and Lemma 1 will be provided in Appendix A.

**Lemma 1.** For i.i.d. particles  $\{\mathbf{x}_i^j\}_{i=1}^n$  with the common generating function  $\mathbb{E}[e^{\Phi(\mathbf{x}; \theta)}]$  that has the Markov property, the empirical measure  $\rho_t$  satisfies the large deviation principle with a rate functional in the form of  $\mathcal{I}_t$ .

**Theorem 1.** Given a base measure  $q$  and a clique potential  $\Phi$ , the density of pGCN in Eq. 1 can be obtained **sufficiently** and **necessarily** by solving the following constrained optimization problem:

$$\begin{aligned} \rho_{t+1} &= \operatorname{argmin}_{\rho} \mathcal{K}(\rho | \rho_t), \\ \text{s.t. } \int \Phi d\rho &= \int \Phi d\mathbb{P}_r, \quad \rho_0 = q, \quad \forall \rho \in \mathcal{P}_{\alpha}^{lin}. \end{aligned} \quad (6)$$

Let  $\theta$  be the Lagrange multiplier integrated in  $\Phi(\mathbf{x}; \theta)$  [11] and ensure that  $\mathbb{E}[e^{\Phi(\mathbf{x}; \theta)}] < \infty$ ; then, the optimization objective 6 can be reformulated as follows (as distinction from Eq. 5,  $l$  represents the LD):

$$\mathcal{I}_t^l = \min_{\rho} \max_{\theta} \left\{ \mathcal{K}(\rho | \rho_t) + \int \Phi(\mathbf{x}; \theta) d\rho - \int \Phi(\mathbf{x}; \theta) d\mathbb{P}_r \right\}. \quad (7)$$

Since  $\nabla_{\mathbf{x}} \log P(\mathbf{x}; \theta) = \nabla_{\mathbf{x}} \Phi(\mathbf{x}; \theta)$ , the SDE iteration of  $\mathbf{x}_t$  in Eq. 4 can be expressed in the Langevin form as follows:

$$\mathbf{x}_{t+1} = \mathbf{x}_t + \nabla_{\mathbf{x}} \log P(\mathbf{x}_t; \theta) + \sqrt{2}\tau_t, \quad (8)$$

where  $\tau_t$  is the gaussian term. By Lemma 1, if we fix  $\theta$ , the sampling scheme in Eq. 8 approaches the KL discrete flow  $\mathcal{I}_t^l$ , and the flow will fluctuate if  $\theta$  varies. Parameter  $\theta$  is updated by calculating  $\nabla_{\theta} \mathcal{I}_t^l$ , which implies that  $\theta$  can dynamically transform the transition map (if we consider the all the learned distributions a transformed version of reference distribution  $q$ ) into the desired form. The sampling process of a pGCN model can be summarized as follows:

$$\begin{cases} \mathbf{x}_{t+1} = \mathbf{x}_t - \left( \frac{\mathbf{x}_t}{\sigma^2} - \nabla_{\mathbf{x}} \Phi(\mathbf{x}_t; \theta) \right) + \sqrt{2}\tau_t, \\ \theta_{t+1} = \theta_t + \nabla_{\theta} \mathbb{E}_{\rho_t}[\Phi(\mathbf{x}; \theta)] - \nabla_{\theta} \mathbb{E}_{\mathbb{P}_r}[\Phi(\mathbf{x}; \theta)], \end{cases} \quad (9)$$

where  $-\mathbf{x}_t/\sigma^2$  is the derivative of initial Gaussian noise  $q$ . Examining the objective function Eq. 7 shows that there is an alternately mechanism involved in updating  $\mathbf{x}_t$  and  $\theta_t$ .

Obviously, the derived Eq. 9 for updating is completely the same as that of MLE in pGCN; thus, optimize  $\rho_t$  to minimize the KL discrete flow  $\mathcal{I}_t$  from this particle perspective, as Theorem 1 has proved, is equivalent to that in its

traditional information theoretical point of view. This theoretically justifies our pGCN reformulation. *i.e.*, the minimum amount of transformations of the reference measure  $q$  (or  $\rho_0$ ). However, such a minimization of the KL divergence might be the cause of the energy unpredictably collapsing to 0; namely, the learned model will reduce to producing the initial noise instead of the desired minimum modification. Hence, if  $\Phi(x, \theta) \leq 0$ , the learned model will tend to degenerate, the images synthesized from pGCN trained by the KL divergence will collapse immediately, and the image quality may barely recover. This is identified as KL-vanishing issue.

## 4 GENERALIZING ENERGY-BASED GENERATIVE CONVNET MODEL

From the particle evolution perspective as discussed above, a pGCN learning process can be interpreted with a KL discrete flow; in turn, the KL vanishing problem becomes manifest and likely causes severe model collapse. To address this problem, our reformulation of pGCN claimed in Sec. 3 provides a principle manner to extend pGCN with the discrete flow; namely, KL divergence term in pGCN could be substituted by an appropriate metric measure under SDE. These still hold for GCN or M-GCN which can be as a pGCN with trainable deep filters. Accordingly, we generalize this KL discrete flow with KL divergence measure into a JKO discrete flow with Wasserstein distance measure in prototype energy-based GCN model, and derive Wasserstein pGCN (w-pGCN) in Sec. 4.1. This JKO discrete flow is connected with the theory of Fokker-Planck Equation and the Wasserstein distance [14].

To further improve its model generalization and its learning capability, we employ a normal distribution as hidden space rather than the original downsampled ground-truth represented reference distribution in multi-scale GCN; considering that the grid-by-grid upscaling functions make the bias accumulated, a trainable non-linear upsampling strategy is proposed. Together with all the above, a generalized Generative ConvNet model (GGCN) is derived in Sec. 4.2.

### 4.1 Wasserstein Prototype GCN Model

Although explaining pGCN from a KL approach is rational from the perspective of the information theory methodology, there is a risk of the KL-vanishing problem as discussed above. The main reason is the non-convergence of the parameter updating mechanism of MLE. Then here in this section, we manage to solve this issue by generalizing the KL discrete flow with KL divergence measure into a JKO discrete flow with Wasserstein distance measure, which can be theoretically proved in particle perspective, and incorporate the Wasserstein JKO discrete flow into pGCN to derive a Wasserstein pGCN model (w-pGCN).

#### 4.1.1 JKO Discrete flow with Wasserstein metric

To avoid the KL-vanishing problem, we would like to introduce the Wasserstein metric driven JKO discrete flow. This flow is annotated as  $\mathcal{J}_t$ . In this particle perspective, we explain this substitution according to [28],  $P_\theta$  in a KL

method can be closer given an empirical measure  $\rho_t$  than the same measure applied with the Wasserstein distance. The closer measure makes the transition of learning more inclined to wrong or collapse location in the energy manifold. Additionally, [29] also claims that a better convergence and approximate results can be obtained since the Wasserstein metric defines a weaker topology. The conclusion that  $\mathcal{I}_t \approx \mathcal{J}_t$  if time step  $t \rightarrow 0$  rationalizes the proposed method (meaning a relatively long sampling process). The proof of this conclusion in the one-dimensional case is presented in [30], [31], [32].

This JKO discrete flow connects the energy model with the theory of Fokker-Planck Equation, which describes the evolution of the probability density function of particle velocity; the required metric in the case of the Fokker-Planck equation is the Wasserstein metric on probability densities [14]. The solution of Fokker-Planck equation is demonstrated as, at each instant in time, the direction of the steepest descent of associated free energy functional, which usually is regarded as discrete gradient flow. Thus here we introduce the Fokker-Planck equation to build the connection. This formulation reveals an appealing, and previously unexplored, the relationship between the Fokker-Planck equation and the associated free energy functional.

Let  $\mathcal{P}$  denote the space of Borel probability measures on any given subset of space  $\mathcal{X}$ , where  $\forall x \in \mathcal{X}$ ,  $x \in \mathbb{R}^d$ . Given some sufficient statistics  $\phi : \mathcal{X} \rightarrow \mathbb{R}$ , scalar  $\alpha \in \mathbb{R}$  and base measure  $q$ , the space of distributions satisfying a linear constraint is defined as  $\mathcal{P}_\alpha^{lin} = \{p, f \in \mathcal{P} : p = fq, f \geq 0, \int p dx = 1, E_p[\phi(x)] = \alpha\}$ . The Wasserstein space of order  $r \in [1, \infty]$  is defined as  $\mathcal{P}_r = \{p \in \mathcal{P} : \int |x|^r dp < \infty\}$ , where  $|\cdot|^r$  denotes the  $r$ -norm on  $\mathcal{X}$ .  $|\mathcal{X}|$  is the number of elements in domain  $\mathcal{X}$ .  $\nabla$  denotes the gradient, and  $\nabla \cdot$  denotes the divergence operator.

**Fokker-Planck Equation.** Let  $F$  be an integral function and  $\delta F / \delta \rho$  denote its Euler-Lagrange first variation; then, the Fokker-Planck equations are as follows:

$$\begin{cases} \partial_t \rho + \nabla \cdot (\rho \nu) = 0 & \text{(Continuity equation)} \\ \nu = -\nabla \frac{\delta F}{\delta \rho} & \text{(Variational condition)} \\ \rho(\cdot, 0) = \rho_0 & \rho_0 \in L^1(\mathbb{R}^d), \rho_0 \geq 0. \end{cases} \quad (10)$$

Compared with Eq. 5, this function models particle density of probability into a continued state [14].

**Wasserstein Metric.** The solution steepest descent, or discrete gradient flow, makes sense only in context with an appropriate metric. The required metric for the Fokker-Planck equation is the Wasserstein metric on probability densities [14]. The Benamou-Brenier form of Wasserstein metric [33] of order  $r$  involves solving the following smooth OT problem over any probabilities  $\mu_1$  and  $\mu_2$  in  $\mathcal{P}_r$ . The solution can be derived by using the continuity equation shown in Eq. 10,

$$\begin{aligned} \mathcal{W}^r(\mu_1, \mu_2) := \min_{\rho_t \in \mathcal{P}_r} \left\{ \int_0^1 \int_{\mathbb{R}^d} |\nu_t|^r d\rho_t dt : \partial_t \rho_t \right. \\ \left. + \nabla \cdot (\rho_t \cdot \nu_t) = 0 \mid \rho_0 = \mu_1, \rho_1 = \mu_2 \right\}, \end{aligned} \quad (11)$$

where  $\nu$  belongs to the tangent space of the manifold (here we suppose particles are moving through a manifold) governed by some potential and associated with curve  $\rho_t$ .

**JKO Discrete Flow.** Following the initial study [14] that shows how Fokker-Planck diffusions of distributions in Eq. 10 are recovered when minimizing entropy functionals according to Wasserstein metric  $\mathcal{W}^2$ , the JKO discrete flow is used by our method to replace the initial KL divergence with the entropic Wasserstein distance  $\mathcal{W}^2 - H(\rho)$ . The function of the flow is as follows:

$$\mathcal{J}_t = \frac{1}{2}\mathcal{W}^2(\rho, \rho_t) + \int \log \rho d\rho + \int \Phi d\rho. \quad (12)$$

#### 4.1.2 Wasserstein Prototype GCN

Wasserstein prototype GCN (w-pGCN) is associated with a JKO discrete flow  $\mathcal{J}_t$  instead of original KL discrete flow p-GCN. Next in this section we will further discuss this replacement and provide a new JKO discrete flow LD optimization objective.

**Remark 1.** The initial Gaussian term  $q$  is left out for convenience to facilitate the derivation; otherwise, entropy  $-H(\rho) = \int \log \rho d\rho$  in Eq. 12 would be written as relative entropy  $\mathcal{K}(\rho | q)$ .

By Theorem 1,  $\mathcal{J}_t$  instead of  $\mathcal{I}_t$  can be calculated approximately, and a steady state will approach Eq. 1. Using  $\mathcal{J}_t$  as a dissipation mechanism instead of  $\mathcal{I}_t$  allows regarding the diffusion Eq. 4 as the steepest descent of clique energy  $\Phi$  and entropy  $-H(P) = \int \log \rho d\rho$  w.r.t. the Wasserstein metric. Solving such an optimization problem using  $\mathcal{W}$  is identical to solving the Monge-Kantorovich mass transfer problem [33].

Using the second mean value theorem for definite integrals, we can approximate the integral in  $\mathcal{W}^2$  (where  $|\nu| \leftarrow |\nabla \Phi|$ ) by two randomly interpolated rectangles:

$$\begin{aligned} \mathcal{W}^2(\rho_{t_0}, \rho_{t_1}) &:= \inf_{\rho_t} \int_{t_0}^{t_1} \int_{\mathbb{R}^d} |\nabla \Phi|^2 d\rho_t dt \\ &\approx (\iota - t_0) \int_{\mathbb{R}^d} |\nabla \Phi|^2 d\rho_{t_0} + (t_1 - \iota) \int_{\mathbb{R}^d} |\nabla \Phi|^2 d\rho_{t_1} \\ &= -\beta \left( (1 - \gamma) \int_{\mathbb{R}^d} |\nabla \Phi|^2 d\rho_{t_0} + \gamma \int_{\mathbb{R}^d} |\nabla \Phi|^2 d\rho_{t_1} \right), \end{aligned} \quad (13)$$

where  $\beta = t_1 - t_0$  parameterizes the time piece, and  $\gamma = \iota/\beta$  ( $0 \leq \gamma \leq 1$ ) represents a random interpolated parameter since  $\iota$  is a random ( $t_0 \leq \iota \leq t_1$ ). Eq. 13 means that the functional derivative of  $\mathcal{W}^2(\rho_{t_0}, \rho_{t_1})$  w.r.t.  $\rho_{t_1}$  is proportional to the following:

$$\frac{\delta \mathcal{W}^2(\rho_{t_0}, \rho_{t_1})}{\delta \rho_{t_1}} \propto |\nabla \Phi|^2, \quad (14)$$

which is exactly the result of Proposition 8.5.6 in [34]. Assume that  $\Phi$  be at least twice differentiable and treat Eq. 14 as the variational condition in Eq. 10; then, plugging Eq. 14 into the continuity equation of Eq. 10 turns the latter into a modified JKO discrete flow in the Fokker-Planck form as follows:

$$\partial_t \rho = \Delta \rho - \nabla \cdot (\rho(\nabla \Phi - \nabla |\nabla \Phi(x)|^2)). \quad (15)$$

Then, the corresponding SDE can be written in the Euler-Maruyama form as follows:

$$x_{t+1} = x_t + \nabla \Phi(x_t) - \nabla |\nabla \Phi(x_t)|^2 + \sqrt{2}\tau_t. \quad (16)$$

By remark 1, if we reconsider the initial Gaussian term  $q$ , the discrete flow of  $x_{t+1}$  in Eq. 16 should be incremented by  $-x_t/\sigma^2$ .

**Remark 2.** If  $\Phi$  is the energy function defined in Eq. 1, then  $\nabla |\nabla \Phi(x)|^2 = 0$ .

The above is a direct result since  $\Phi(x, \theta)$  defined in pGCN only involves inner product, piecewise linear ReLU and other linear operations, and the second derivative is obviously 0. Since  $\nabla |\nabla \Phi(x)|^2 = 0$ , the time evolution of density  $\rho_t$  in Eq. 15 and sample  $x_t$  in Eq. 16 will reduce to Eq. 10 and Eq. 8, respectively. Thus, the SDE of  $x_t$  holds by default, i.e., retains the Langevin form while the gradient of the model parameter  $\theta_t$  does not vanish.

Similar to the parameterized KL flow  $\mathcal{I}_t^l$  defined in Eq. 7, we propose a similar form for the JKO case. Using Eq. 13 and Eq. 14, the **final optimization objective function**  $\mathcal{J}_t^l$  can be formulated as follows:

$$\begin{aligned} \mathcal{J}_t^l &= \min_{\rho} \max_{\theta} \left\{ -\frac{\beta}{2} (1 - \gamma) \int_{\mathbb{R}^d} |\nabla_x \Phi(x; \theta)|^2 d\rho_t \right. \\ &\quad - \frac{\beta}{2} \gamma \int_{\mathbb{R}^d} |\nabla_x \Phi(x; \theta)|^2 d\rho + \int \log \rho d\rho \\ &\quad \left. + \int \Phi(x; \theta) d\rho - \int \Phi(x; \theta) d\mathbb{P}_r \right\}. \end{aligned} \quad (17)$$

Given the entire discussion above, the learning progress of w-pGCN can be constructed by gradient ascent of  $\theta$ , i.e.,  $\nabla_{\theta} \mathcal{J}_t^l$ . The calculation steps of the formulation are summarized in Eq. 18:

$$\begin{cases} x_{t+1} = x_t - \left( \frac{x_t}{\sigma^2} - \nabla_x \Phi(x_t; \theta) \right) + \sqrt{2}\tau_t, \\ \theta_{t+1} = \theta_t + \nabla_{\theta} \mathbb{E}_{\rho_t} [\Phi(x; \theta)] - \nabla_{\theta} \mathbb{E}_{\mathbb{P}_r} [\Phi(x; \theta)] \\ \quad - \frac{\beta}{2} (1 - \gamma) \nabla_{\theta} \mathbb{E}_{\rho_{t-1}} [|\nabla_x \Phi(x; \theta)|^2] \\ \quad - \frac{\beta}{2} \gamma \nabla_{\theta} \mathbb{E}_{\rho_t} [|\nabla_x \Phi(x; \theta)|^2]. \end{cases} \quad (18)$$

Equation 18 indicates that the gradient of  $\theta$  determined in the Wasserstein manner is being added with some soft gradient norm constraints between the last two iterations. Such a gradient norm has the following advantages compared with the original iterative process (Eq. 9). First, the norm  $|\nabla_x \Phi(x; \theta)|^2$  serves as the constant speed geodesic connecting  $\rho_t$  with  $\rho_{t+1}$  in the manifold spanned by  $\mathbb{P}_{\theta}$  and  $\mathbb{P}_r$ , which may provide a speedup of convergence. Second, it can be interpreted as a soft force counteracting the original gradient and preventing the entire learning process from stopping. Finally, in experiments we observe that it can preserve internal structural information of data.

Considering that the simple difference between GCN and pGCN is whether the filter parameter  $w$  is trained synchronously, with the similar method, Wasserstein GCN (w-GCN) could be derived to specifically illustrate the particle evolution perspective of GCN learning with JKO discrete flow. Details are provided in Algorithm 1.

## 4.2 Generalized Generative ConvNet Model

We reformulation the conventional energy-based pGCN model from a particle evolution perspective, explain theoretically pGCN in KL discrete flow in Sec. 3, and generalize the formulation of pGCN from KL discrete flow to JKO discrete flow driven by Wasserstein metric in Sec. 4.1. Considering that GCN is a filter-trainable version of pGCN, in this section, we further generalize the pGCN/w-pGCN with

**Algorithm 1** Learning Wasserstein GCN

---

**Require:** Training data  $\{y^i, i = 1, \dots, N\}$ ; Langevin steps  $L$ ; training iterations  $T$ ; learning rates  $\lambda$

**Ensure:** Synthesized data  $\{x^i, i = 1, \dots, M\}$ ; estimated parameters  $\theta, w$

```

1: Initialize  $x_0^i \leftarrow 0$ 
2: for  $t = 1$  to  $T$  do
3:    $H^{obs} \leftarrow \frac{1}{N} \sum_i^N \nabla_{\theta_t} \Phi(y^i)$ 
4:    $R^{obs} \leftarrow \frac{1}{N} \sum_i^N \nabla_{w_t} \Phi(y^i)$ 
5:   for  $j = 1$  to  $\mathcal{L}$  do
6:      $\mathcal{G} \leftarrow \nabla_{x_{t \times \mathcal{L} + j - 1}} \Phi(x_{t \times \mathcal{L} + j - 1})$ 
7:      $\mathcal{S} \leftarrow \frac{x_{t \times \mathcal{L} + j - 1}}{\sigma^2}$ 
8:     Sample  $\tilde{\Sigma} \leftarrow \mathcal{N}(0, \sigma^2 \cdot \mathbf{I}_d)$ 
9:      $x_{t \times \mathcal{L} + j} \leftarrow x_{t \times \mathcal{L} + j - 1} + \frac{\delta^2}{2}(\mathcal{G} - \mathcal{S}) + \delta \tilde{\Sigma}$ 
10:   end for
11:    $H^{syn} \leftarrow \frac{1}{M} \sum_i^M \nabla_{\theta_t} \Phi(x_{(t+1) \times L}^i)$ 
12:    $R^{syn} \leftarrow \frac{1}{M} \sum_i^M \nabla_{w_t} \Phi(x_{(t+1) \times L}^i)$ 
13:    $\mathcal{P}_t \leftarrow \frac{1}{M} \sum_i^M \nabla_{\theta_t} |\nabla_{x_{(t+1) \times L}} \Phi(x_{(t+1) \times L}^i)|^2$ 
14:    $\mathcal{P}_{t-1} \leftarrow \frac{1}{M} \sum_i^M \nabla_{\theta_t} |\nabla_{x_{t \times L}} \Phi(x_{t \times L}^i)|^2$ 
15:   Sample  $\gamma \sim U[0, 1]$ 
16:   Update  $\theta_{t+1} \leftarrow \theta_t + \lambda \cdot (H^{obs} - H^{syn}) - \frac{\beta}{2}((1 - \gamma)\mathcal{P}_{t-1} + \gamma\mathcal{P}_t)$ 
17:   Update  $w_{t+1}^k \leftarrow w_t^k + \lambda \cdot (R_k^{obs} - R_k^{syn})$ 
18: end for

```

---

JKO discrete flow and derive our Generalized Generative ConvNet Model (GGCN). This generalization strategy is non-trivial, rather than simply extending pGCN/w-pGCN in a deep GCN model with JKO discrete flow.

GCN is regarded as a one-scale model and its multi-scale version M-GCN [13] is proposed to speed up the model learning. It is demonstrated that the M-GCN is especially inefficient in training since there is a pile of several GCNs in different grids all of which have to be estimated through consuming MCMC sampling. Besides, after applying JKO discrete flow to each grid of GCN, the generative capability and generalized property is still greatly limited by the linear upscale functions and downsampled referenced distribution. This is the main reason that GCNs are rarely trained on large-scale datasets. Thus, to improve the learning efficiency we use a non-linear upsampling function to mimic the updating and sampling process of GCNs in the M-GCN, which to some extent improves the model generalization property. Next we expand the initial reference distribution in the first grid of M-GCN to a random gaussian reference distribution (which is invalid without non-linear trainable upsampling); finally, we introduce a learning hidden space mechanism, which further improves the learning stability. The whole GGCN can be learned in a symmetrical parameter estimation cycle.

#### 4.2.1 Generalized Generative ConvNet Model

M-GCN is a pile of several of GCNs with different scales, as shown in subfigure (a) of Fig.3. Its learning and synthesis process is through learning each GCN grid-by-grid with LD sampling. Therefore, when in high dimensional data synthesis, the low learning efficiency grows significantly which also results in low synthesis quality. We thus consider an equivalent learnable and upscaling structure to mimic

the learning process of middle grids of GCNs in M-GCN. To further simplify the model and its learning procedure, we then only reserve the last grid of GCN in the M-GCN and extend the model to learn the distribution from a hidden space.

**Nonlinear Learnable Upsampling.** Although a multi-grid mechanism indeed improves the synthesis quality slightly [13], it mostly depends on hundreds of MCMC sampling steps, which brings many inefficiencies especially in synthesizing high dimensional data. Noted that upscaling in M-GCN is simply a linear operation, we presume that substitution of the several grids of GCN by layers of learnable nonlinear upsampling functions will speed up the learning procedure since it mimics the sampling process by simply minimizing the error between the sampled synthesized data and the real-world data. Learning the hidden space mechanism is further proposed (the same process as learning  $x$  in GCN), which makes the whole model can be learned symmetrically.

**Hidden Space Mapping.** Two one-scale GCNs at each end as shown in Fig.3 are not necessary. Since the property that learning a GCN is to model the input data distribution, if we extend the input to a random sample from Gaussian distributed in the same dimension as the downsampled real data, then the function of the first GCN becomes modeling a given random distribution. Thus this first GCN can be omitted and the whole pipeline turns into the structure as shown in the right subfigure (b) of Fig.3. Suppose the original sample synthesis a generating process, a mapping from a projection space of real data distribution to real distribution is learned through MCMC, and the latter process can be considered as a learning generator process. This process is likewise learning generator in GAN, thus spontaneously, we expand the input space to the hidden space.

Given a probability distribution with density function  $p(x)$ , we assume  $g(\zeta; \xi)$  to be the nonlinear upsampling network, where  $\zeta$  represents a sampled initial gaussian noise, and  $\xi$  denotes parameters. The given information only includes random noise (from an unknown real-world distribution  $q^*$ ), trainable function  $g$  and its derivative  $\nabla_{\xi} g$ . Our learning objective is to find an optimal  $\zeta$  satisfying  $\zeta \sim q^*$  such that the output  $x = g(\zeta; \xi)$  matches the objective probability density function  $p(x)$ . Parameters are learned by the following:

$$\xi_{t+1} \leftarrow \underset{\xi}{\operatorname{argmin}} \sum_i^M \|g(\zeta_i; \xi_t) - x'_i\|_2^2, \quad (19)$$

where  $x'_i = x_i + \varepsilon \Delta x_i$ , is the synthesized sample,  $M$  is the batch size and  $\Delta x_i$  denotes the gradient of  $x_i$ .

#### 4.2.2 Symmetrical Learning Strategy

As shown in subfigure (a) of Fig.3, we simplify the learning procedure to a trade-off between learning GCN and a learning hidden space strategy with non-linear sampling functions. The training strategy is illustrated in the subfigure (b) of Fig.3, and it is a symmetrical structure learned with the same iterative method. To be more specific, we define the hidden variable  $\zeta$  with non-linear upsampling function  $g$  as a **generator** and the GCN in GGCN as a **synthesizer**. As a matter of fact, the whole model is still a GCN with



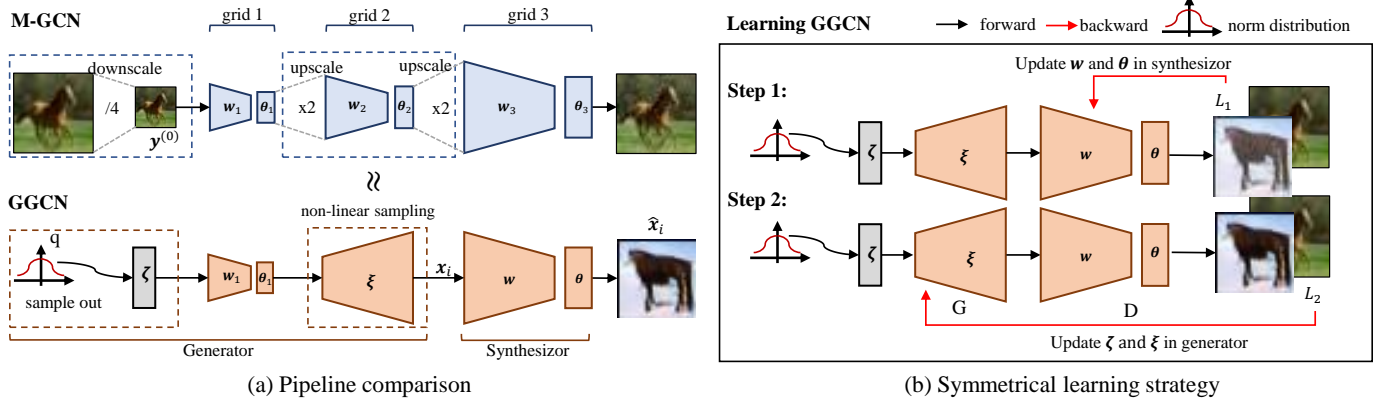


Fig. 3. Example pipeline of M-GCN and GGCN with three grids. As shown in the upper left subfigure, a multi-scale GCN is a tiled structure of several one-scale GCNs. In GGCN, due to the introduction of hidden space mapping, the first grid can be omitted since it is equivalent to an auto-encoder (or we apply this part with  $1 \times 1$  convolutional layers, there will be no loss in performance). Our non-linear sampling improves the sampling efficiency compared with M-GCN with time-consuming MCMC sampling. The right part is the training strategy guideline of GGCN.  $L_1$  and  $L_2$  are the response losses computed in the same method but with different parts of networks fixed. Noted that all the GCN learning step in GGCN is applied with Wasserstein method and amortized sampling process.

a parameterized mapping that synthesizes  $x$  by updating the hidden space; therefore the synthesis  $x$  is a middle result of the whole model learning and sampling. Noted that the GCN part in GGCN is modified to wGCN as the final model for implementation. The detailed algorithm can be found in Algorithm 2. As shown in Algorithm 2 line 4, an LD is still necessary, which may result in a relatively long leaning process, we thus introduce an amortized sampling to GGCN, denoted as GGCN\*.

**Learning the Hidden Space.** Even if the nonlinear up-sampling function  $g(\zeta; \xi)$  is introduced and an acceleration method is applied to GCN, the whole framework still has a disadvantage of high sensitivity to random initialization, network structure, and hyperparameter selection.

We consider this to be mainly caused by the possibly incorrect hidden space initialization  $y^{(0)}$ , *i.e.*, the downsampled real data for the first grid of M-GCN. Thus, we apply a hidden space optimization strategy proposed by [35], [36] that is capable of capturing the connection between the noise vector and the signal and preventing the learning procedure from going astray. Hidden variable  $\zeta$  is updated by the gradient of reconstruction loss in nonlinear upsampling function as follows:

$$\min_{\zeta_i} \sum_{i=1}^M [\min_{\zeta_i \in \mathcal{Z}} \mathcal{L}(g(\zeta_i), \hat{x}_i)], \quad (20)$$

where  $\mathcal{L}$  denotes a final approximating reconstruction loss. Note that optimizing either  $\zeta$  or network parameter  $\xi, w$  will not influence the Wasserstein process of updating  $\theta$ , see algorithm 2.

The GGCN model has the following advantages: (1) the generator  $g(\zeta)$  mimics the sampling process by simply minimizing the error between the sampled synthesized data and the real-world data; (2) the low-dimensional hidden space can be mapped into any high-dimensional training data by this function (also means friendly to high dimensional data synthesis); (3) higher learning efficiency is gained compared with previous M-GCN; (4) the accumulating divergence scale-by-scale in M-GCN can be

#### Algorithm 2 Symmetrical Learning Strategy for GGCN

**Require:** Training data  $\{y^i, i = 1, \dots, N\}$ ; Langevin steps  $L$ ; training iterations  $T$ ; learning rates  $\lambda$

**Ensure:** Synthesized data  $\{x^i, i = 1, \dots, M\}$ ; estimated parameters  $\theta, w, \xi$

- 1: Sample  $\zeta_t^i \sim q$
- 2: **for**  $t = 1$  **to**  $T$  **do**
- 3:  $x_t^i \leftarrow G(\zeta_t^i; \xi_t)$
- 4: Get  $\hat{x}_t^i$  by Langevin sampling respect with  $D$ .
- 5:  $\theta_{t+1} \leftarrow \nabla_{\theta} L_1(D(\hat{x}_t^i), D(y^i))$
- 6:  $w_{t+1} \leftarrow \nabla_w L_1(D(\hat{x}_t^i), D(y^i))$   
(Line 4-6 are the same with learning  $w$  and  $\theta$  in 1)
- 7:  $\xi_{t+1} \leftarrow \nabla_{\xi} L_2(D(G(\zeta_t^i; \xi_t)); \theta_{t+1}, w_{t+1})$
- 8:  $\zeta_{t+1}^i \leftarrow \nabla_{\zeta} L_2(D(G(\zeta_t^i; \xi_t)); \theta_{t+1}, w_{t+1})$
- 9: **end for**

reduced in GGCN and therefore gains improvements on synthesis quality.

**Amortized Langevin Dynamic Sampling.** The traditional MCMC algorithm is an inefficient inference technique for approximating energy-based probabilistic models. A GGCN still needs a relatively long time to perform the iteration to obtain an approximation, since  $\forall x'$  in Eq. 19 are synthesized by several rounds of sampling in the synthesizer (a GCN). To further accelerate our model, and inspired by an amortized SVGD method proposed by [15] that is claimed to maximally reduce the KL divergence, we use an amortized dynamic sampling method to speed up the sampling progress.

If scalar  $\varepsilon$  in Eq.19 is sufficiently small, the optimization of  $g$  can be rewritten into the least-squares form. Using the Taylor expansion, we obtain  $g(\zeta; \xi_t) \approx g(\zeta_i; \xi_t) + \partial_{\xi} g(\zeta_i; \xi_t)(\xi - \xi_t)$ . Since  $x_i = g(\zeta_i; \xi_t)$ , we obtain the following:

$$\|g(\zeta_i; \xi_t) - x'_i\|_2^2 \approx \|\partial_{\xi} g(\zeta_i; \xi_t)(\xi - \xi_t) - \varepsilon \Delta x_i\|_2^2. \quad (21)$$

After being rewritten in the least-squares form, the opti-



mization problem becomes as follows:

$$\begin{aligned} \xi^{t+1} &\leftarrow \xi_t + \varepsilon \Delta \xi_t, \\ \Delta \xi_t &= \underset{u}{\operatorname{argmin}} \sum_{i=1}^M \|g(\zeta_i; \xi_t)u - \varepsilon \Delta x_i\|_2^2 \end{aligned} \quad (22)$$

Due to involving the matrix inverse operation, this parameter estimation routine is inevitably computationally intensive; hence, one step of the gradient descent computation will provide a sufficient approximation. The final updating equation is as follows:

$$\xi^{t+1} \leftarrow \xi_t + \varepsilon \sum_{i=1}^K \partial_{\xi} g(\zeta_i; \xi_t) \Delta x_i. \quad (23)$$

This updating equation defines a reconstruction approximation loss  $\mathcal{L}$ , thus we can apply this loss to Eq. 20. Although the this equation is a rough approximation [37], it is both efficient and effective in the implementation phase because if  $\varepsilon$  is small, one step of the gradient descent method reaches relatively close to the optimal solution. We will update  $\xi$  by following a more explicit form that literally maximizes the gradient ascent  $\mathbb{E}_{\zeta}[\log p(g(\zeta; \xi))]$  because it is equivalent to equation 23. In this form,  $g(\zeta; \xi)$  is trained to maximize  $\log p(x)$  instead of sampling from  $P$ . The learning strategy of  $\theta$  remains as in Eq. 18 and  $w$  is learned through Eq. 3.

## 5 EXPERIMENTS

In this section, we conduct extensive experimental evaluations of our proposed models on four benchmarks: CelebA [38], SUN [39], LSUN-Bedroom [40], CIFAR-10 [41], and Tiny ImageNet [38]. Firstly, we elaborate the experimental settings in Section 5.1, and provide detailed quantitative comparison results of our proposed models in Section 5.2 and Section 5.3. Then, empirical model analysis and assessment are discussed in Section 5.4 and the superiority of less sampling training for our proposed models are demonstrated in Section 5.5. Finally, we extend our models to another task, *i.e.*, image inpainting and interpolation in Section 5.6.

### 5.1 Experimental Settings

**Datasets.** Four benchmark datasets are selected for our experimental evaluation: one face dataset (*i.e.*, CelebA) and three natural image datasets (*i.e.*, LSUN [39], CIFAR-10, Tiny ImageNet).

- **CelebA** is a widely used large-scale face dataset of human celebrities, which contains over 10,000 images. We only use its face-center-cropped version.
- **SUN** [39] has 899 scene categories and 130,519 images. It is a large dataset mainly for scene recognition.
- **LSUN-Bedroom** [40] contains only one bedroom category and total one million images.
- **CIFAR-10** consists of 60,000 32x32 colour images in 10 categories, with 6,000 images per class.
- **Tiny ImageNet** [42] is a light version of ImageNet dataset. This dataset has 200 classes out of 1,000 classes of ImageNet and 500 images in each category.

Considering that some large-scale datasets have no category information (namely label, such as CelebA and LSUN-Bedroom), we only implement unconditional training on these datasets while others with label information can be carried out with conditional learning (input vector is the concatenation of random Gaussian noise and embedded label vector).

**Evaluation metrics.** Two metrics are chosen to evaluate our proposed models, *i.e.*, inception scores (IS) [43] and response distance.

- **Inception score** is a prevalent metric for generative models, which measures the diversity and the reality of the generated sample. It uses the network called Inception v2 [44] pretrained on ImageNet [45] to capture the classifiable properties of samples.
- **Response distance** [10]  $R$  is defined as follows:

$$R = \frac{1}{K} \sum_{k=1}^K \left| \frac{1}{N} \sum_{i=1}^N F_k(x^i) - \frac{1}{M} \sum_{i=1}^M F_k(y^i) \right|,$$

where  $F_k$  denotes the  $k$ th filter. The smaller  $R$  is, the better the generated results since  $R \propto \max_{\theta} (\mathbb{E}_{\theta}[F(y^i)] - \mathbb{E}_{P_{\theta}}[F(x^i)])$ , which implies that  $R$  provides an approximation of the divergence between the target data distribution and the generated data distribution. Furthermore, with Eq. 2, the faster  $R$  declines, the faster  $\theta$  converges. This metric is a reflection of energy in the particle perspective. The more energy gained, the larger response distance shown.

**Learning settings.** For pGCN, we follows the default settings in [12]. For w-pGCN,  $\lambda$  is set to  $1e^{-3}$ ;  $\delta$  is 0.2 for CelebA and 0.15 for LSUN-Bedroom and CIFAR-10. The default setting of  $\sigma$  is 0.01,  $\beta$  is 60, the number of learning iterations  $T$  is 100, the step number  $L$  of LD sampling within each learning iteration is 50, and the batch size  $N$  and  $M$  are 100. The implementation of  $\Phi(x)$  in w-pGCN uses the first four convolutional layers of a pretrained VGG-16 [46] but is fixed during training.

For proposed variants of our models (*i.e.*, GGCN, GGCN<sup>-</sup>, GGCN<sup>-\*</sup> and GGCN<sup>\*</sup>), we set  $\delta$  to 1.0, the learning rate of generators and synthesizers to  $2e^{-4}$  and batch size  $N$  to 100; the step number of Langevin learning iteration  $L$  is among [10, 40]. The corresponding generator and hidden variables will be updated after every 4 iterations of updating the synthesizer and generate images. The generator is a ResNet50 [47] based auto-encoder and the synthesizer is simply a ResNet50. There is also a shallower network version for GGCNs, detail structural information is provided in Appendix.

The dimension hidden variable  $\zeta$  in GGCNs is 128 for ImageNet and CIFAR-10, 256 for CelebA, and its learning rate  $\varepsilon$  is  $1e^{-3}$  on ImageNet,  $3e^{-3}$  on CelebA, and  $1e^{-2}$  on CIFAR-10. All the parameters are leaned by Adam optimizer, except that  $\zeta$  is learned by SGD. Usually, there will be a total of 500 or 1,000 epochs of training, and a memory replay buffer similar to that in [48] is used. This image buffer serves as a one-step advance initialization of the next sampling step.

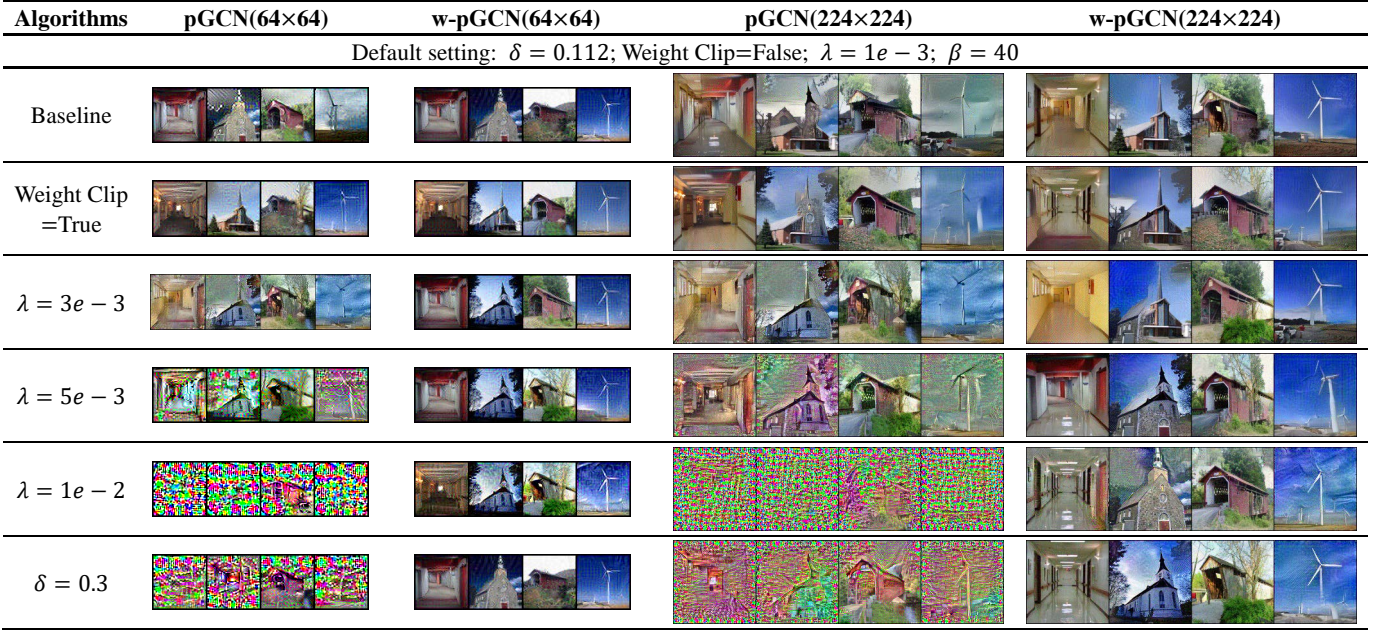


Fig. 4. Synthesized results of pGCN and w-pGCN under various hyperparameter settings, where the “Baseline” represents the models with default settings. For each image scale ( $64 \times 64$ ,  $224 \times 224$ ), w-GCN always generates better images than GCN. Furthermore, under different hyperparameter settings, w-pGCN still presents a stable learning ability. On the contrary, pGCN fails to address the sample collapse or artifacts problem derived from model collapse. For example, with small changes in learning rate  $\lambda$ , the generated image quality of pGCN significantly deteriorates with severe image artifacts. Overall, the stability of learning a w-pGCN model apparently surpasses that of pGCN. If we consider the model collapse an unstable particle energy dissipation phenomenon, the Wasserstein method effectively improves this shortcoming in pGCN since different learning strategies that seriously interfere pGCN synthesis have much slighter effect on w-pGCN.

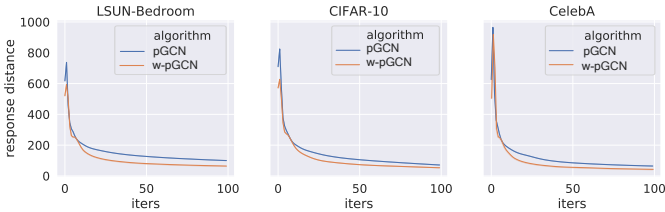


Fig. 5. Averaged learning curves of response distance  $R$  on CelebA, LSUN-Bedroom, and CIFAR-10 datasets. The sooner the curves of response distance converge to zero, the more stable the training process of the respective model. All red curves corresponding to w-pGCN converge quicker than does the blue original pGCN curve. The response distance is a reflection of energy. A quicker and closer response distance to 0 implies a better learning state and higher quality of synthesis.

## 5.2 Comparison on pGCN and w-pGCN

To address the model collapse problem, Wasserstein distance under the particle evolution conditions is introduced for conventional pGCN and GCN models, deriving w-pGCN and w-GCN. To demonstrate its effectiveness, we mainly provide our proposed w-pGCN comparison results with pGCN in this section. Extensive experiments are conducted on CelebA, LSUN-Bedroom and CIFAR-10 datasets under various experimental settings. These settings involve different learning rates, different input image scales, and with/without weight clipping.

In Fig.4, less sample synthesized results of pGCN and w-pGCN under various hyperparameter settings are shown. For each image scale ( $64 \times 64$  or  $224 \times 224$ ), w-pGCN always generates better images than pGCN. Furthermore, under different hyperparameter settings, w-pGCN still presents

a stable learning ability. On the contrary, GCN fails to address the sample artifacts problem resulted from model collapse. For example, as shown from the third to fifth row in Fig.4, with small changes of learning rate  $\lambda$ , the generated image quality of pGCN significantly deteriorates with severe image artifacts. Obviously, the learning of w-pGCN is less sensitive to hyperparameter tuning and its stability of learning surpasses that of pGCN.

A similar performance is also illustrated with the averaged learning curves of pGCN and w-pGCN in Fig.5. In Fig.5, it is observed that the averaged learning curves of w-pGCN are all apparently closely converging to 0 on three datasets, which implies a faster and more stable learning of w-pGCN compared with pGCN according to that the smaller the response distance is, the less divergence between real distribution and estimated distribution.

Thus, if we consider the model collapse an unstable particle energy dissipation phenomenon, the Wasserstein method effectively improves this shortcoming in pGCN since different learning strategies that seriously interfere pGCN synthesis have much slighter effects on w-pGCN.

As demonstrated in Fig.4 and Fig.5, without the Wasserstein method, the synthesized results would certainly collapse after several iterations of pGCN learning. Similarly, this model collapse also occurs for other variants of pGCN, e.g., GCN or M-GCN. As shown in Fig.6 (a), most synthesized images contain gray spot areas which are obvious indications of model collapse. Conversely, variants of our proposed w-pGCN, e.g., w-MGCN and GGCN, greatly improve the image generation quality as shown in Fig.6 (b)-(d), demonstrating a stable learning ability.



Fig. 6. Comparison of synthesized results for the CelebA dataset. Images from (a) to (d) show the results of M-GCN, wM-GCN, GGCN<sup>-\*</sup> and GGCN<sup>\*</sup>, respectively. From (a) to (b) we find that Wasserstein method can eliminate the model collapse phenomenon in (a), but there are still some twisting drawbacks in synthesized samples as shown in (b); The amortized sampling with non-linear upsampling applied model GGCN no twisting as shown in (c), however, a little blurring remains. The learning hidden space mechanism will further improve the blurring, as manifested in (d) that the final results are much more clear.

TABLE 1

LCN stands for learning CNN filters; JKO is JKO discrete flow (namely the Wasserstein learning mechanism); MS represents Multi-scale; NLU means applying layers of non-linear upsampling functions which cannot coexist with MS; HS is an abbreviation of hidden space, here means extend the input to a random space and leave out the first grid of GCN; AMS is the annotation of amortized sampling method; LHS is learning the hidden space.

Model	LCN	JKO	MS	NLU	HS	AMS	LHS
pGCN							
w-pGCN		✓					
GCN	✓						
wGCN	✓	✓					
M-GCN	✓		✓				
wM-GCN	✓	✓	✓				
GGCN	✓	✓		✓	✓		✓
GGCN <sup>*</sup>	✓	✓		✓	✓	✓	✓
GGCN <sup>-</sup>	✓	✓		✓	✓		
GGCN <sup>-*</sup>	✓	✓		✓	✓	✓	

### 5.3 Comparison on the proposed GGCN

Our w-pGCN reformulates the conventional energy-based models (*i.e.*, pGCN and GCN) from particle evolution perspective, further generalizes the conventional GCN approach by introducing JKO discrete flow with Wasserstein distance measure and derives w-pGCN variants (*i.e.*, wM-GCN, GGCN<sup>-</sup> and GGCN<sup>\*</sup>) to solve more practical problems. Detailed experimental results of these models are elaborated in the following. The models related with detailed methods can be found in Tab.1.

#### 5.3.1 Experimental Results on CelebA

We provide synthesized results of M-GCN, wM-GCN, GGCN<sup>-\*</sup> and GGCN<sup>\*</sup> on CelebA dataset in Fig.6. After time-consuming iterations of training, an M-GCN still suffers from collapse issue even with carefully finetuning. As demonstrated in Fig.6(a), most synthesized images of M-GCN contain gray spot areas which obviously indicate the model collapse issue. In Fig.6(b), it is observed that our proposed wM-GCN alleviates this issue by applying the JKO discrete flow and the gray spots are not shown any more in the synthesized results. However, those synthesized images

of wM-GCN are still blurry and distorted and artifices or ghosts are present since a mere Wasserstein learning cannot solve the problem of accumulating divergence between real data distribution and estimated data distribution from scale to scale.

Accordingly, our proposed GGCN introduces JKO discrete flow with Wasserstein distance measure and further improves the image quality, shown in Fig.6(c). Compared with Fig.6(b), these results have less twisted lines, faces are more realistic. Considering the twisting issue in the synthesis might be caused by the accumulating divergence through different scales in M-GCN, GGCN<sup>-\*</sup> leverages non-linear upsampling functions, maps the input to a hidden space, and manages to conquer this problem. Compared with results from those methods, the images resulting from the proposed model GGCN<sup>\*</sup> in Fig.6(d) are clearest, least distorted and comparable with real human face images.

#### 5.3.2 Experimental Results on CIFAR-10

We compare our proposed models with state-of-the-art methods in Table 2. Considering available category labels of CIFAR-10 dataset, the performance results of inception score on both conditional and unconditional learning are provided. Compared with base model pGCN, GGCN<sup>\*</sup> obtains respectively 2.51 and 2.15 gains in the unconditional and conditional settings. In comparison with state-of-the-art GAN based methods, our proposed still demonstrates a significant improvement in inception score in unconditional/conditional settings. For example, GGCN gains around 0.6 improvements over DCGAN. Further, higher quality images with more realistic natural scenes are generated by GGCN than those of DCGAN, as demonstrated in Fig.8(b). In those images of GGCN, objects in these images such as cars, horses, and airplanes are easily be recognized.

#### 5.3.3 Experimental Results on Tiny ImageNet

Tiny ImageNet synthesis results are provided on two image scales, *i.e.*,  $32 \times 32$  and  $64 \times 64$ . A visualization of conditional learning results for both sizes are shown in Fig.9. Considering that the capacity of ImageNet is much larger than CelebA and CIFAR-10 datasets and its images contain relatively complicated objects and unclear background, these



TABLE 2

Inception scores on CIFAR-10. The upper are the results of unconditional learning, the downside are conditional learning. The state-of-art conditional result of Improved GAN reported in [43] is 8.09, but this result has not been reproduced so far. Among the explicit models, GGCN outperforms most methods on both datasets. The inception score of all real-world images of CIFAR-10 is  $11.24 \pm 0.11$ .

Method	Inception Score
<b>CIFAR-10 without labels</b>	
pGCN [18]	$4.28 \pm 0.05$
Improved GAN	$4.36 \pm 0.05$
w-pGCN [18]	$5.52 \pm 0.13$
ALI [49]	$5.34 \pm 0.05$
DCGAN [37]	$6.16 \pm 0.07$
GGCN*(ours)	<b><math>6.79 \pm 0.08</math></b>
<b>CIFAR-10 with labels</b>	
pGCN [18]	$4.95 \pm 0.05$
WINN-5CNNs [50]	$5.58 \pm 0.05$
w-pGCN [18]	$6.05 \pm 0.13$
SteinGAN [15]	$6.35 \pm 0.05$
M-GCN [13]	$6.57 \pm 0.05$
DCGAN [13]	$6.58 \pm 0.05$
GGCN*(ours)	$7.01 \pm 0.05$
GGCN(ours)	<b><math>7.10 \pm 0.07</math></b>

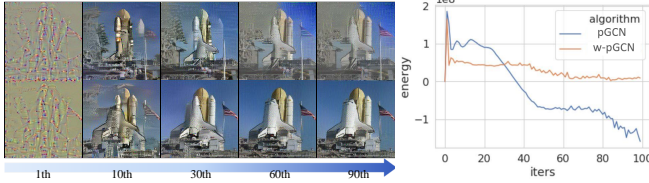


Fig. 7. The left part of the synthesis results from pGCN and one proposed model w-pGCN. The sample from the upper row crashes at the beginning of the iteration while the other row provides a more stable synthesis. The right curves respectively represent the energy of these two GCNs at each time step, as shown that the energy curve of p-GCN is in greater ups and downs and finally results in less than 0.

features challenge the learning of generative models on ImageNet, and the generations on this dataset are not as satisfying as the former two large scale datasets. However, GGCN manages to generate images with clear edges and textures, especially in scale  $64 \times 64$ , some objects and scenes can even be identified, such as the fruits and cars in the third row and mountains from the first row in Fig.9(a).

## 5.4 Model Analysis and Assessment

### 5.4.1 Improvement of Training Stability

A comparison with pGCN shown in Fig.7 that illustrates the typical evolution of generated samples demonstrates an improvement of training stability. The generated images are almost identical in the beginning; however, images produced by our algorithm are undergoing the expected changes after 30 iterations, while those produced by pGCN deteriorate. Quantitatively, the curves in Fig.5 are calculated by averaging across the entire dataset. The w-pGCN method has a lower cost according to response distance  $R$ ; namely, a direct  $l_1$  critic in section.5.1 of filter banks between synthesized samples and target samples is smaller and decreases more steadily. More specifically, our algorithm has mostly

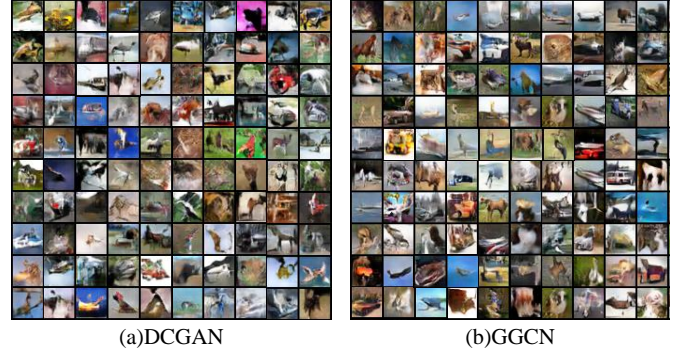


Fig. 8. Unconditional generation of GGCN and DCGAN on CIFAR-10. Objects of (b) can be identified more easily than those in (a).

solved the model collapse problem of pGCN because it not only ensures the closeness of the generated samples and the “ground-truth” samples but also stabilizes the learning phase of model parameter  $\theta$ . The three plots clearly show that the quantitative measures are strongly correlated with qualitative visualizations of generated samples. In the absence of model collapse, we obtain results that are comparable to or even better than those of pGCN.

Since GGCN can be regarded as a GCN with a more complex sampling mechanism, the Wasserstein method that applied to GCN is also implemented to GGCN. Results of Fig.6(a) to Fig.6(d) shows that the collapse issue has been completely solved in GCNs with Wasserstein method since no more gray spot appearing in the synthesis results from any proposed models. This implies that the original energy dissipation process is rectified to be more stable. Another steadiness improvement is manifested in the generalization of GCN. Compare the results of Fig.6(b) 6(c), the context of the latter is more sensibly organized. As we have discussed in section 4.2.1, the divergence or learning error will be accumulated as the learning scale increases in M-GCN. Obviously, the Wasserstein method merely helps with the collapse issue. Thus we own this improvement to the non-linear upsampling functions and the extension to hidden space mechanisms which largely reduce the accumulating error by combining the estimating and modification of the hidden variable.

### 5.4.2 Improvement of Image Generation Quality

According to our performance measured by response distance  $R$ , the quality of image synthesis is improved. This measurement corresponds to the iterative learning process of both pGCN and w-pGCN. The learning curves presented in Fig.5 represent the observations of the overall datasets’ synthesis. The curves also imply that w-pGCN converges faster than pGCN.

From subfigures (b) of Fig.6, we found that even applied with Wasserstein learning method in training method, most result images of M-GCN are in the condition of either unclear outline edge, or a total distorted face, or being full of unknown spots which make picture extremely dirty. On the contrary, images produced by GGCN\* (Fig.6(c)) and with learning hidden space mechanism (Fig.6(d)) are both reasonably mixed, sensibly structured and brightly colored and less distorted. Especially the synthesized results



Fig. 9. Conditional generation using images of Tiny ImageNet resized to  $32 \times 32$  (b) and  $64 \times 64$  (a) by GGCN.

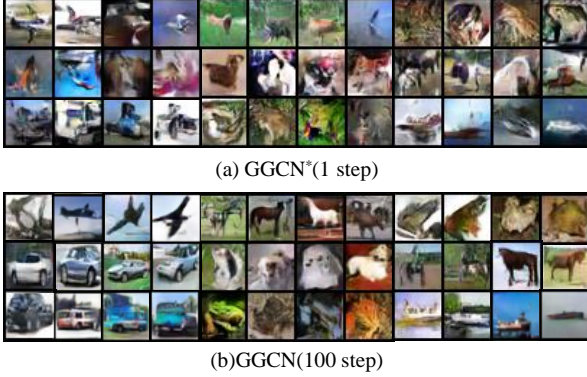


Fig. 10. The group (a) is synthesized by the model using one-step sampling which is equivalent with applying the amortizing sampling; results in (b) correspond to 100-step sampling. The upper group has a lower inception score than the other results.

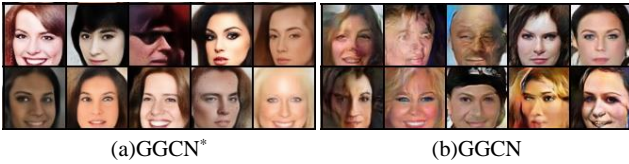


Fig. 11. Results of group(a) are produced by GGCN\* while those of (b) are from GGCN. On the contrary of Fig.10, GGCN without amortized sampling mechanism performs worse on dataset CelebA.

from GGCN\* maintain more clear contexts than GGCN\* which implies LHS can improve the image quality from this respect.

On the other hand, compared with traditional GCN or M-GCN, GGCN\* can be more efficiently trained on large datasets such as CIFAR-10 and ImageNet. Since the inception score is shown to correlate well with human scoring of the realism of generated images from the generative model on CIFAR-10 dataset, higher inception score than other energy-based model (e.g. WINN [50]) to some extent implies this new GGCN synthesizes better quality than others. This conclusion also can be drawn from Fig.8 which is showing that visually GGCN generates more identified objects from DCGANs with CIFAR-10.

#### 5.4.3 Discussion

Noticed that the amortized sampling method has a controversy that may influence the model performance. We consider this amortized sampling a cost-effective acceleration scheme, since performance declines in some situations if it is implemented. We suspect this is due to the

approximation of Taylor's expansion in 21. Therefore we particularly conduct a comparison experiment of GGCN and GGCN\* on CIFAR-10 with conditional learning. The visual results are presented in Fig.10, where group (a) are the results of GGCN\*, (b) GGCN. Though GGCN\* can be trained efficiently, GGCN can synthesize better. Nevertheless, this conclusion will not sustain on CelebA, since we found that GGCN\* outperforms GGCN on this dataset, as shown in Fig.11. We conjecture this is due to the property of the datasets, as distinguishing features for generation on CIFAR-10 is benefited while to some extent is the burden to that of CelebA. Thus amortized sampling is not recommended to implement on the generation of CIFAR-10 etc..

### 5.5 Less Sample Training

It is generally known that recent popular generative models such as GANs are all trained on the massive dataset, thus the energy-based models at the beginning are blamed for the inefficiency on training massively. However, those largely learned models are mostly cannot be trained on the small training set. Quick and accurate learning is required in less sample training pGCN can perfectly achieve with this target while DCGAN, as a representative of popular generative models, somehow has a really hard time converging on this learning task after epochs of training.

We conduct less sample learning on w-pGCN compared with DCGAN. Most primitive energy-based model is performed in this scenario thus we w-pGCN can achieve even better results (no collapse anymore). The performance of DCGAN in modeling only a few images is shown in Fig.13, where for a fair comparison we duplicate the input images several times to a total of 10,000 to match the training environment of DCGAN. The compared w-pGCN model is trained using our method. The DCGAN's training procedure stops as it converges, but results showing quite likewise. Besides, all the comparison experiments in section 5.2 are the less sample training results.

### 5.6 Image Inpainting and Interpolation

To fully validate our proposed models, we further extend our models to another two tasks, i.e., image inpainting and interpolation on the CelebA dataset, which maintains a superior performance on both experiments.

In the inpainting experiment on GGCN\*, the image with the mask is regarded as the hidden space latent variable mapped by the generator to the real-world data space. If an upsampling generator with a random hidden variable



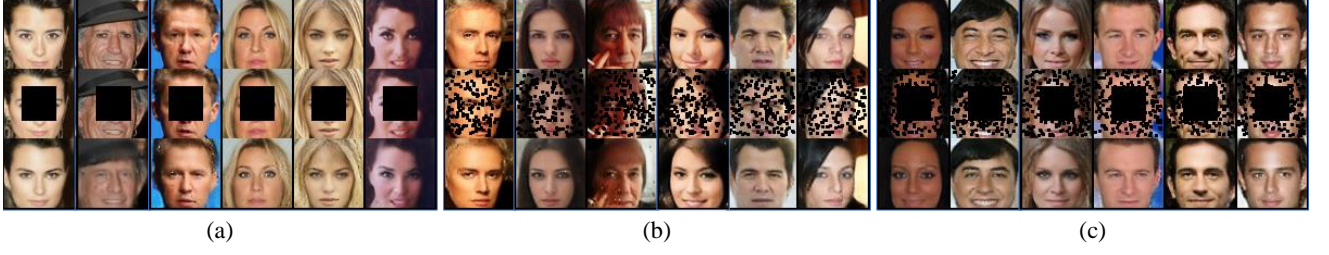


Fig. 12. Inpainting generation examples of GGCN\*. (a) is square mask inpainting, (b) is the random spot mask and (c) is the combination of the former two. As shown, GGCN\* can complement the missing space with a reasonable context.



Fig. 13. The left image in the first row shows the input images selected from the SUN dataset. The right image in the first row presents the outputs of DCGAN. The right image in the last row displays the outputs of our method. All the GCNs can synthesize real and authentic images with less sample efficiently, while after thousands of epoch, GAN can barely fit the real data distribution and generates ambiguous results.

TABLE 3

We evaluate MSE (mean square error), FID (Frechet inception distance score [19]), SSIM (structural similarity index measure) and PSNR (peak-signal-to-noise ratio) to GGCN\* on dataset CelebA for inpainting task. The experiment settings are the default settings of CelebA synthesis in section 5.3.1. All criteria show that the synthesis results of three masks from GGCN\* are close to real images.

Mask Type	MSE	FID	SSIM	PSNR
Spot Mask	0.0033	25.44	0.954	30.410
Square Mask	0.0041	30.69	0.934	30.095
Combine Two	0.0046	25.03	0.940	30.039

used as input can be trained to complete the masked images as other generative models. GGCN\* adopts an autoencoder of ResNet50 as the generator, whose input is an image multiplied by a mask array. We apply three types of masks to evaluate our model: a square box, random spots and a combination of the two. As shown in Fig.12, the model infers reasonable and texture-level smooth contents to fill the blank space. The larger the blank space is, the more different the generated image from the original one. We also evaluate our inpainting results with frequently used criteria, the figures in Tab.3 imply that GGCN\* can synthesis realistic faces.

In the interpolation experiment, we randomly pick two hidden variable vectors denoted by  $\zeta$  with 256 dimensions, clip their values to the range of  $[-1, 1]$ , and then linearly generate 10 intermediate vectors using the equation  $\zeta_c = c(\zeta - \zeta_0)/10 + \zeta_0$ . Here in Fig.14, we display some



Fig. 14. Image interpolation results of the proposed GGCN\* on the CelebA dataset. Every interpolation has 8 midpoints. The transfer process has been tested across gender, between gender, and on different or identical face attributes, such as hair color, face pose, etc.

typical interpolation results of our model. As shown, no matter how different faces the picked two hidden variables can be synthesized to, the middle generated faces of inter vectors can keep the form with the facial property continuously change. For example, in the first row, the faces at two ends are generated from the picked two random vectors, the left is a woman with left face direction, while the other one is a man slightly face to the right. The faces between them form a transition from female to male, direction from left to the right. The example shows a transition crossing gender and direction, we also provide transitions between different hair cuts, expressions, skin color, etc.

## 6 CONCLUSION

In this paper, we track and rederive the origin of the pGCN model from the perspective of particle evolution and discover the potential factors that may lead to a deteriorating quality of generated samples and instability of model training, *i.e.*, the vanishing problem inherent in minimization of the KL divergence. Based on this discovery, we propose the w-pGCN model by reformulating the KL discrete flow in the pGCN model into the JKO flow and prove empirically that this strategy can overcome the above mentioned



deficiencies. The Wasserstein method can be applied to other energy-based GCN models. Additionally, to overcome challenges of time consumption and model collapse during synthesis, we propose another model called GGCN which is modified from an M-GCN but can be regarded as a one-scale GCN. GGCN is designed and trained on a specific symmetrical learning structure. Experiments are performed to demonstrate the superiority of the proposed Wasserstein method and GGCN models, and comparable results show that the Wasserstein method can significantly mitigate the vanishing issue of energy-based models and produce more visually appealing results. Moreover, the final model GGCN can be further accelerated through an cost-effective amortized sampling mechanisms. Our investigation on the generalization of energy-based GCN models presents an appealing research topic from the particle evolution perspective and is expected to provide an impetus for the present research on EBMs.

## APPENDIX A

**Theorem 1.** Given a base measure  $q$  and a clique potential  $\Phi$ , the density of pGCN in Eq. 1 can be obtained **sufficiently** and **necessarily** by solving the following constrained optimization problem:

$$\begin{aligned} \rho_{t+1} &= \underset{\rho}{\operatorname{argmin}} \mathcal{K}(\rho \mid \rho_t), \\ \text{s.t. } \int \Phi d\rho &= \int \Phi d\mathbb{P}_r, \quad \rho_0 = q, \quad \forall \rho \in \mathcal{P}_\alpha^{\text{lin}}. \end{aligned} \quad (24)$$

*Proof.* **Necessity** can be proven using MEP by calculating  $\partial_\rho \mathcal{I}_t^i$  iteratively:

$$\begin{aligned} \lim_{t \rightarrow \infty} \rho_{t+1} &= \frac{1}{Z} e^{\omega_t \cdot \Phi} \rho_t \\ &= \frac{1}{Z} e^{(\omega_t + \omega_{t-1}) \cdot \Phi} \rho_{t-1} \\ &= \dots = \frac{1}{Z} e^{\Phi(x; \theta)} q. \end{aligned}$$

**Sufficiency:** Recalling the Markov property in Eq. 1, we can write the inner product as a sum of feature responses w.r.t. different cliques; then, the shared pattern activation  $h = \max(0, x_i^t)$  can be approximated by the Dirac measure as follows:

$$\begin{aligned} \sum_{k=1}^K h(\langle x_i^t, w_k \rangle + b_k) &\approx \sum_{k=1}^K \delta_{x_i^t} \sum_{j=1}^C x_i^t(j) w_k(j) \\ &\propto \delta_{x_i^t} \sum_{j=1}^C x_i^t(j). \end{aligned}$$

The result coincides with the empirical measure of  $x_i^t$ , so the proof of **sufficiency** turns into that of Lemma 1 that is completed elsewhere.  $\square$

**Proof of Lemma 1** Under the Gaussian reference measure a pGCN model has the piecewise Gaussian property, as summarized in Proposition 1. This proposition is a reformulation of Theorem 1 and implies that different pieces can be regarded as different generating samples acting as Brownian particles.

**Proposition 1.** Equation 3 is piecewise Gaussian, and on each piece the probability density can be written as follows:

$$P(x; \theta) \propto \exp \left[ -\frac{1}{4} \|x - y\|^2 \right] \quad (25)$$

where  $y = \sum_{k=1}^K \delta_k \theta_k$  is an approximate reconstruction of  $x$  in one part of the data space by a linear transformation involving inner products of model parameters and a piecewise linear activation function (ReLU).

By Proposition 1, each particle (image piece) in a pGCN model has the transition kernel of the Gaussian form (equation 25). It describes the probability of a particle moving from  $x \in \mathbb{R}^d$  to  $y \in \mathbb{R}^d$  in time  $t > 0$ . Let a fixed measure  $\rho_0$  such as the Gaussian distribution be the initial measure of  $n$  Brownian particles  $\{x_0^i\}_{i=1}^n$  at time 0.

The Sanov theorem shows that the empirical measure  $\rho_t = \frac{1}{n} \sum_{i=1}^n \delta_{x_t^i}$  of such transition particles satisfies Langevin dynamics process (LDP) with rate functional  $\mathcal{K}(\rho_t \mid \rho_0)$ , i.e.,

$$\frac{1}{n} \sum_{i=1}^n \delta_{x_t^i} \sim \exp[-\mathcal{K}(\rho_t \mid \rho_0)]. \quad (26)$$

Specifically, each Brownian particle has  $|\mathcal{X}|$  internal subparticles that are independent and belong to different cliques. Let  $C$  denote the number of cliques; the Cramer's theorem states that for i.i.d. random variables  $x_i(j)$  with a common generating function  $\mathbb{E}[e^{\Phi(\theta)}]$ , the empirical mean  $\frac{1}{C} \sum_{j=1}^C x_i(j)$  satisfies LDP with rate functional given by the Legendre transformation of  $\mathbb{E}[e^{\Phi(\theta)}]$ ,

$$\frac{1}{C} \sum_{j=1}^C x_i(j) \sim \exp \left[ \theta - \mathbb{E}[\Phi(\theta)] \right]. \quad (27)$$

Since the empirical measure of  $x_t^i$  is simply the empirical mean of the Dirac measure, i.e.,  $\delta_{x_t^i} \frac{1}{C} \sum_{j=1}^C x_i(j)$ , the empirical measure over all particles is shown to be as follows:

$$\begin{aligned} \frac{1}{n} \sum_{i=1}^n \delta_{x_t^i} \frac{1}{C} \sum_{j=1}^C x_i^t(j) &\stackrel{\text{Eq. 26, 27}}{\sim} \exp[-\mathcal{K}(\rho_t \mid \rho_0)] \cdot \exp \left[ \theta - \mathbb{E}[\Phi(\theta)] \right] \\ &\propto \exp \left[ -\left[ \mathcal{K}(\rho_t \mid \rho_0) + \mathbb{E}[\Phi(\theta)] \right] \right]. \end{aligned}$$

where the exponent is exactly the KL discrete flow  $\mathcal{I}$ . Thus, the empirical measure of the activation patterns of all particles satisfies LDP with rate functional  $\mathcal{I}_t$  in discrete time.

## APPENDIX B

### NETWORK STRUCTURE DETAILS

**GGCN v0.** This network structure is the GGCN v0 for synthesizing results in Fig.6 (c) and Fig.11 (a). As shown that there is a ResNet50 version v1 by which we achieve best results of CIFAR-10 and Tiny ImageNet results, but this will be provided in code.

TABLE 4

Detailed network structure information of GGCN v0. Network structure v0 is used to obtain all of experimental examples shown in (Fig. 6). Structure v1 is a pile of three ResNets that is built to attain the best performance. Note that the network structure is shared between GGCN and GGCN+LHS. For more details, please refer the code of which the link is listed in the footnote.

Operation	Kernel	Step Size	Heat map	Norm	Activation
$G_x(\eta) - 512 \times 1 \times 1$ input					
Deconv	$4 \times 4$	$1 \times 1$	512	✓	Leaky ReLU
Deconv	$7 \times 7$	$2 \times 2$	256	✓	Leaky ReLU
Deconv	$5 \times 5$	$2 \times 2$	256	✓	Leaky ReLU
Deconv	$7 \times 7$	$2 \times 2$	128	✓	Leaky ReLU
Deconv	$2 \times 2$	$1 \times 1$	64	✓	Leaky ReLU
Conv	$1 \times 1$	$1 \times 1$	3	×	Sigmoid
$D(x) - 3 \times 64 \times 64$ input					
Conv	$2 \times 2$	$1 \times 1$	64	✓	Leaky ReLU
Conv	$7 \times 7$	$2 \times 2$	128	✓	Leaky ReLU
Conv	$5 \times 5$	$2 \times 2$	256	✓	Leaky ReLU
Conv	$7 \times 7$	$2 \times 2$	256	✓	Leaky ReLU
Conv	$4 \times 4$	$1 \times 1$	512	✓	Leaky ReLU
$E(x) - 512 \times 1 \times 1$ input					
Deconv	$4 \times 4$	$1 \times 1$	512	✓	Leaky ReLU
Deconv	$7 \times 7$	$2 \times 2$	256	✓	Leaky ReLU
Deconv	$5 \times 5$	$2 \times 2$	256	✓	Leaky ReLU
Deconv	$7 \times 7$	$2 \times 2$	128	✓	Leaky ReLU
Deconv	$2 \times 2$	$1 \times 1$	64	✓	Leaky ReLU
Conv	$1 \times 1$	$1 \times 1$	3	×	Sigmoid
Optimizer	Adam ( $\lambda = 10^{-4}$ , $\beta_1 = 0.5$ )				
Batch Size	100				
Number of iterations	500				
Leaky ReLU tilt	0.02				
Dropout	0.0				
Weight initialization	Isotropic Gaussian ( $\mu = 0$ , $\sigma = 0.02$ ), Constant(0)				

## REFERENCES

- [1] S. C. Zhu, Y. Wu, and D. Mumford, "Filters, random fields and maximum entropy (frame): Towards a unified theory for texture modeling," *International Journal of Computer Vision*, vol. 27, no. 2, pp. 107–126, 1998.
- [2] J. Baek, G. J. McLachlan, and L. K. Flack, "Mixtures of factor analyzers with common factor loadings: Applications to the clustering and visualization of high-dimensional data," *IEEE transactions on pattern analysis and machine intelligence*, vol. 32, no. 7, pp. 1298–1309, 2009.
- [3] Y. Wei, Y. Tang, and P. D. McNicholas, "Flexible high-dimensional unsupervised learning with missing data," *IEEE Transactions on Pattern Analysis and Machine Intelligence*, 2018.
- [4] J. Liang, J. Yang, H.-Y. Lee, K. Wang, and M.-H. Yang, "Sub-gan: An unsupervised generative model via subspaces," in *Proceedings of the European Conference on Computer Vision (ECCV)*, 2018, pp. 698–714.
- [5] I. Goodfellow, J. Pouget-Abadie, M. Mirza, B. Xu, D. Warde-Farley, S. Ozair, A. Courville, and Y. Bengio, "Generative adversarial nets," in *Advances in Neural Information Processing Systems*, 2014, pp. 2672–2680.
- [6] D. P. Kingma and M. Welling, "Auto-encoding variational bayes," *International Conference on Learning Representations (ICLR)*, Banff, AB, Canada, Conference Track Proceedings, 2014.
- [7] L. Dinh, D. Krueger, and Y. Bengio, "Nice: Non-linear independent components estimation," *International Conference on Learning Representations (ICLR)*, 2015.
- [8] Y. LeCun, S. Chopra, R. Hadsell, M. Ranzato, and F. Huang, "A tutorial on energy-based learning," *Predicting structured data*, vol. 1, no. 0, 2006.
- [9] A. Krizhevsky, I. Sutskever, and G. E. Hinton, "Imagenet classification with deep convolutional neural networks," in *Advances in neural information processing systems*, 2012, pp. 1097–1105.
- [10] J. Xie, Y. Lu, S.-C. Zhu, and Y. Wu, "A theory of generative convnet," in *International Conference on Machine Learning*, 2016, pp. 2635–2644.
- [11] S. C. Zhu, Y. N. Wu, and D. Mumford, "Minimax entropy principle and its application to texture modeling," *Neural Computation*, vol. 9, no. 8, pp. 1627–1660, 1997.
- [12] Y. Lu, S.-C. Zhu, and Y. N. Wu, "Learning frame models using cnn filters," *Proceedings of the Thirtieth AAAI Conference on Artificial Intelligence*, Phoenix, Arizona, USA., 2016.
- [13] R. Gao, Y. Lu, J. Zhou, S.-C. Zhu, and Y. Nian Wu, "Learning generative convnets via multi-grid modeling and sampling," in *Proceedings of the IEEE Conference on Computer Vision and Pattern Recognition*, 2018, pp. 9155–9164.
- [14] R. Jordan, D. Kinderlehrer, and F. Otto, "The variational formulation of the fokker-planck equation," *SIAM journal on mathematical analysis*, vol. 29, no. 1, pp. 1–17, 1998.
- [15] D. Wang and Q. Liu, "Learning to draw samples: With application to amortized mle for generative adversarial learning," *arXiv preprint arXiv:1611.01722*, 2016.
- [16] L. D. Landau and E. M. Lifshitz, *Course of theoretical physics*. Elsevier, 2013.
- [17] J. Dai, Y. Lu, and Y.-N. Wu, "Generative modeling of convolutional neural networks," *International Conference on Learning Representations (ICLR)*, 2015.
- [18] X. Cai, Y. Wu, G. Li, Z. Chen, and L. Lin, "Frame revisited: An interpretation view based on particle evolution," in *Proceedings of the AAAI Conference on Artificial Intelligence*, vol. 33, 2019, pp. 3256–3263.
- [19] M. Heusel, H. Ramsauer, T. Unterthiner, B. Nessler, and S. Hochreiter, "Gans trained by a two time-scale update rule converge to a local nash equilibrium," in *Advances in Neural Information Processing Systems*, 2017, pp. 6626–6637.
- [20] A. Radford, L. Metz, and S. Chintala, "Unsupervised representation learning with deep convolutional generative adversarial networks," *International Conference on Learning Representations (ICLR)*, 2016.
- [21] D. P. Kingma, T. Salimans, R. Jozefowicz, X. Chen, I. Sutskever, and M. Welling, "Improving variational inference with inverse autoregressive flow," *Advances in Neural Information Processing Systems*, 2016.
- [22] L. Dinh, J. Sohl-Dickstein, and S. Bengio, "Density estimation using real nvp," *International Conference on Learning Representations (ICLR)*, 2017.
- [23] J. Xie, Y. Lu, S.-C. Zhu, and Y. N. Wu, "Cooperative training of descriptor and generator networks," *arXiv preprint arXiv:1609.09408*, 2016.
- [24] T. Kim and Y. Bengio, "Deep directed generative models with energy-based probability estimation," *arXiv preprint arXiv:1606.03439*, 2016.
- [25] L. Younes, "Parametric inference for imperfectly observed gaussian fields," *Probability Theory and Related Fields*, vol. 82, no. 4, pp. 625–645, 1989.
- [26] M. A. Peletier, "Energies, gradient flows, and large deviations: a modelling," 2012.
- [27] S. Whitaker, "Flow in porous media i: A theoretical derivation of darcy's law," *Transport in porous media*, vol. 1, no. 1, pp. 3–25, 1986.
- [28] G. Montavon, K.-R. Müller, and M. Cuturi, "Wasserstein training of restricted boltzmann machines," in *Advances in Neural Information Processing Systems*, 2016, pp. 3718–3726.
- [29] M. Arjovsky, S. Chintala, and L. Bottou, "Wasserstein generative adversarial networks," in *International Conference on Machine Learning*, 2017, pp. 214–223.
- [30] S. Adams, N. Dirr, M. A. Peletier, and J. Zimmer, "From a large-deviations principle to the wasserstein gradient flow: a new micro-macro passage," *Communications in Mathematical Physics*, vol. 307, no. 3, pp. 791–815, 2011.
- [31] M. H. Duong, V. Laschos, and M. Renger, "Wasserstein gradient flows from large deviations of many-particle limits," *ESAIM: Control, Optimisation and Calculus of Variations*, vol. 19, no. 4, pp. 1166–1188, 2013.
- [32] M. Erbar, Matthias anErbar, J. Maas, M. Renger *et al.*, "From large deviations to wasserstein gradient flows in multiple dimensions," *Electronic Communications in Probability*, vol. 20, 2015.
- [33] J.-D. Benamou and Y. Brenier, "A computational fluid mechanics solution to the monge-kantorovich mass transfer problem," *Numerische Mathematik*, vol. 84, no. 3, pp. 375–393, 2000.
- [34] L. Ambrosio, N. Gigli, and G. Savaré, *Gradient flows: in metric spaces and in the space of probability measures*. Springer Science & Business Media, 2008.
- [35] T. Han, Y. Lu, S.-C. Zhu, and Y. N. Wu, "Alternating back-propagation for generator network," in *Thirty-First AAAI Conference on Artificial Intelligence*, 2017.
- [36] P. Bojanowski, A. Joulin, D. Lopez-Paz, and A. Szlam, "Optimizing the latent space of generative networks," *Proceedings of International Conference on Machine Learning (ICML)*, 2017.

- [37] Q. Liu and D. Wang, "Learning deep energy models: Contrastive divergence vs. amortized mle," *arXiv preprint arXiv:1707.00797*, 2017.
- [38] Z. Liu, P. Luo, X. Wang, and X. Tang, "Deep learning face attributes in the wild," in *Proceedings of the IEEE International Conference on Computer Vision*, 2015, pp. 3730–3738.
- [39] J. Xiao, J. Hays, K. A. Ehinger, A. Oliva, and A. Torralba, "Sun database: Large-scale scene recognition from abbey to zoo," in *Computer vision and pattern recognition (CVPR), 2010 IEEE conference on*. IEEE, 2010, pp. 3485–3492.
- [40] F. Yu, Y. Zhang, S. Song, A. Seff, and J. Xiao, "Lsun: Construction of a large-scale image dataset using deep learning with humans in the loop," *arXiv preprint arXiv:1506.03365*, 2015.
- [41] A. Krizhevsky and G. Hinton, "Learning multiple layers of features from tiny images," Citeseer, Tech. Rep., 2009.
- [42] O. Russakovsky, J. Deng, H. Su, J. Krause, S. Satheesh, S. Ma, Z. Huang, A. Karpathy, A. Khosla, M. Bernstein, A. C. Berg, and L. Fei-Fei, "ImageNet Large Scale Visual Recognition Challenge," *International Journal of Computer Vision (IJCV)*, vol. 115, no. 3, pp. 211–252, 2015.
- [43] T. Salimans, I. Goodfellow, W. Zaremba, V. Cheung, A. Radford, and X. Chen, "Improved techniques for training gans," in *Advances in Neural Information Processing Systems*, 2016, pp. 2234–2242.
- [44] C. Szegedy, V. Vanhoucke, S. Ioffe, J. Shlens, and Z. Wojna, "Rethinking the inception architecture for computer vision," in *Proceedings of the IEEE conference on computer vision and pattern recognition*, 2016, pp. 2818–2826.
- [45] J. Deng, W. Dong, R. Socher, L.-J. Li, K. Li, and L. Fei-Fei, "Imagenet: A large-scale hierarchical image database," in *Computer Vision and Pattern Recognition (CVPR), 2009. IEEE Conference on*. IEEE, 2009, pp. 248–255.
- [46] K. Simonyan and A. Zisserman, "Very deep convolutional networks for large-scale image recognition," *International Conference on Learning Representations (ICLR)*, 2015.
- [47] K. He, X. Zhang, S. Ren, and J. Sun, "Deep residual learning for image recognition," in *Proceedings of the IEEE conference on computer vision and pattern recognition*, 2016, pp. 770–778.
- [48] V. Mnih, K. Kavukcuoglu, D. Silver, A. Graves, I. Antonoglou, D. Wierstra, and M. Riedmiller, "Playing atari with deep reinforcement learning," *arXiv preprint arXiv:1312.5602*, 2013.
- [49] D. Warde-Farley and Y. Bengio, "Improving generative adversarial networks with denoising feature matching," *International Conference on Learning Representations (ICLR)*, 2017.
- [50] K. Lee, W. Xu, F. Fan, and Z. Tu, "Wasserstein introspective neural networks," in *The IEEE Conference on Computer Vision and Pattern Recognition (CVPR)*, June 2018.



**Xu Cai** received his B.S. degree of computer science and technology from XiDian University, Xian, China, and Masters degree from Sun Yat-Sen University. He is currently pursuing his Ph.D degree at the School of Computing at National University of Singapore. His current research interest is mainly theoretical machine learning.



**Guanbin Li** currently an associate professor at the School of Data and Computer Science, Sun Yat-sen University. He received his Ph.D. degree from the University of Hong Kong in 2016. He was a recipient of a Hong Kong Postgraduate Fellowship. His current research interests include computer vision, image processing, and deep learning. He has authored and co-authored more than 20 papers in top-tier academic journals and conferences. He serves as an area chair for the conference of VISAPP. He has served as a reviewer for numerous academic journals and conferences, such as TPAMI, TIP, TMM, TC, TNNLS, CVPR2018 and IJCAI2018.



**Yang Wu** received the B.S. degree of applied mathematics from South China University of Technology, Guangzhou, China. She is currently pursuing her Ph.D degree at the School of Data and Computer Science of Sun Yat-Sen University, advised by Prof. Liang Lin. Her current research interests include computer vision and machine learning, particularly in generative model and embodied tasks.



**Pengxu Wei** received the B.S. degree in computer science and technology from the China University of Mining and Technology, Beijing, China, in 2011 and the Ph.D. degree from University of Chinese Academy of Sciences in 2018. Her current research interests include visual object recognition, detection and latent variable learning. She is currently a research scientist at Sun Yat-sen University.



**Liang Lin** Liang Lin is a Full Professor at Sun Yat-sen University, and the CEO of DMAI. He served as the Executive R&D Director and Distinguished Scientist of SenseTime Group from 2016 to 2018, taking charge of cutting-edge technology transferring into products. He has authored or co-authored more than 200 papers in leading academic journals and conferences (e.g., TPAMI/IJCV, CVPR/ICCV/NIPS/ICML/AAAI). He is an associate editor of IEEE Trans, Human-Machine Systems and IET Computer Vision. He served as Area Chairs for numerous conferences such as CVPR and ICCV. He is the recipient of numerous awards and honors including Wu Wen-Jun Artificial Intelligence Award for Natural Science, ICCV Best Paper Nomination in 2019, Annual Best Paper Award by Pattern Recognition (Elsevier) in 2018, Best Paper Dimond Award in IEEE ICME 2017, Google Faculty Award in 2012, and Hong Kong Scholars Award in 2014. He is a Fellow of IET.